TUDelft

Delft University of Technology

Depth-averaged unsteady RANS simulation of resonant shallow flows in lateral cavities using augmented WENO-ADER schemes

Navas-Montilla, A.; Juez, C.; Franca, M. J.; Murillo, J.

Citation (APA)
Navas-Montilla, A., Juez, C., Franca, M. J., & Murillo, J. (2019). Depth-averaged unsteady RANS simulation of resonant shallow flows in lateral cavities using augmented WENO-ADER schemes. *Journal of Computational Physics*, *395*, 511-536. https://doi.org/10.1016/j.jcp.2019.06.037

Important note
To cite this publication, please use the final published version (if applicable).
Please check the document version above.

Depth-averaged unsteady RANS simulation of resonant shallow flows in lateral cavities using augmented WENO-ADER schemes

A. Navas-Montilla [1], C. Juez[2], M. J. Franca [3], J. Murillo[4]

[1] *anavas@unizar.es, Fluid Mechanics Department-LIFTEC, CSIC-Universidad de Zaragoza.*
[2] *carmelo.juez@upm.es, Fluid Mechanics Department, ETSIDI, Universidad Politécnica de Madrid.*
[3] *m.franca@un-ihe.org, Water Science and Engineering department, IHE-Delft Institute for Water Education and Department of Hydraulic Engineering, Delft University of Technology.*
[4] *Javier.Murillo@unizar.es, Fluid Mechanics Department-LIFTEC, CSIC-Universidad de Zaragoza.*

Abstract

Turbulent shallow flows are characterized by the presence of horizontal large-scale vortices, caused by local variations of the velocity field. Apart from these 2D large vortices, small scale 3D turbulence, mainly produced by the interaction of the flowing water with the solid boundaries, is also present. The energy spectrum of turbulent shallow flows shows the presence of a 2D energy cascade at low wave numbers and a 3D energy cascade at high wave numbers, with a well-defined separation region between them. Horizontal flow movements (e.g. 2D large-scale vortical structures) at low wave numbers mostly determine the hydrodynamic behavior of these flows. Moreover, the generation of standing waves often occurs closely associated to the interaction of 2D horizontal flows with lateral boundaries, this is the case of seiches. To adequately reproduce these phenomena, a mathematical and numerical model able to resolve 2D turbulence is required. We herein show that depth-averaged (DA) unsteady Reynolds averaged Navier Stokes (URANS) models based on the Shallow Water Equations (SWE) are a suitable choice for the resolution of turbulent shallow flows with sufficient accuracy in an affordable computational time. The 3D small-scale vortices are modelled by means of diffusion terms, whereas the 2D large-scales are resolved. A high order numerical scheme is required for the resolution of 2D large eddies. In this work, we design a DA-URANS model based on a high order augmented WENO-ADER scheme. The mathematical model and numerical scheme are validated against observation of complex experiments in an open channel with lateral cavities that involve the presence of resonant phenomena (seiching). The numerical results evidence that the model accurately reproduces both longitudinal and transversal resonant waves and provides an accurate description of the flow field. The high order WENO-ADER scheme combined with a SWE model allows to obtain a powerful, reliable and efficient URANS simulation tool.

Keywords:
Shallow flows; turbulence; shock capturing; lateral cavities; seiching;

1. Introduction

Shallow water flows are of great interest in civil and environmental engineering. They appear in a wide variety of scenarios ranging from open channels to coastal areas [1, 2]. The water depth in these environmental flows is characterized by being much smaller than the horizontal scale. The turbulence produced in such flows is characterized by two different and coexistent scales of turbulent structures: the 2D turbulence (with length scales much larger than the water depth) and the 3D turbulence (with length scales smaller than the water depth) [3]. Local variations of the velocity field promote the generation of horizontal 2D large-scale coherent vortices. These macro vortical structures

play a relevant role in several aspects of hydro-morphological and biological interest: the conveyance of fine sediments in suspension [4], the transport of pollutants [5] or the mass exchange of nutrients between the flow and the aquatic biota [6]. In addition to 2D macro horizontal vortices, small scale 3D turbulent vortices, produced by the interaction of the flowing water with the solid boundaries and in 2D shear layers, co-exist in environmental shallow flows. They participate in the vertical mass and momentum transfer between the bottom and the flow surface.

The co-existance of 2D and 3D turbulent scales is reflected in the energy spectrum of the shallow flow turbulence. The energy spectrum of such flows displays the presence of a 2D energy cascade at low wave numbers and a 3D energy cascade at high wave numbers, with a well-defined separation region between them [3, 7].

Besides the turbulent nature of shallow flows, another important characteristic of these flows is the existence of a free surface. This free surface is the boundary between the water body and the air above it. It may deform in response to physical intrinsic mechanisms that govern the flow (e.g. it is influenced by the presence of turbulence, wind shear and bed topography). In free surface flows, surface gravity waves usually appear and may determine the hydrodynamic pattern within the flow [8]. This additional feature of shallow water turbulence involves additional energy dissipation mechanism. A particular type of gravity waves are standing resonant waves that appear in bounded flows, called seiches [9]. There is a wide range of spatial scales at which seiches may appear: ranging from centimeters (e.g. seiche in lateral cavities of river banks [9]) to kilometers (e.g. seiche in lakes, bays or harbours [10]). The understanding of seiches is relevant to determine the hydro-morphological interactions between the main stream flow and the lateral cavities of river banks and the consequences of these to mass and momentum transfer [11].

Concerning the mathematical modelling and numerical simulation of free surface shallow flows, multiple approaches have been proposed by the scientific community in the past decades. The use of 3D models with advanced turbulence modelling techniques, such as Reynolds averaged Navier Stokes (RANS) models, large eddy simulation (LES) or direct numerical simulation (DNS), has allowed complex turbulent flows to be simulated with accuracy [12]. However, the use of 3D models is computationally costly and handling the presence of the free surface is not a trivial numerical task. Most numerical techniques (specially for the LES approach) ignore free surface deformations and they use the so-called rigid lid approximation [13]. By using this approach, gravity waves are represented as vertical pressure fluctuations but the deformation of the free surface cannot be tracked, and is numerically simpler than other numerical approaches that aim at computing the physical and real free surface deformation (e.g. interface tracking methods and interface capturing methods [14]). A more recent hybrid approach considers a two-phase LES models that accurately resolve the interface between water and air [15].

A rather different approach for the simulation of free surface shallow flows is the use of 2D depth-averaged models. Such models, involving a significantly lower computational cost, are able to reproduce the propagation of gravity waves and to account for turbulent fluctuations. They are useful for the simulation of large domains, which are virtually unaffordable by means of LES methods. The shallow water equations (SWE) are a hyperbolic system of conservation laws that describe the propagation of nonlinear gravity waves. They can also model additional physical processes by means of extra source and diffusion terms (e.g. friction, bottom topography, turbulence) [16, 17].

The most common approach to handle turbulence for the SWE is the RANS methodology [18, 19, 20, 21], which aims at the resolution of flow mean quantities by modelling the full turbulence spectrum, including the large scales. The fluctuating terms are not resolved, though their effect in the transport of mean quantities is included in the equations by means of a closure formulation that allows to model the Reynolds stress term in terms of the mean flow. This closure formulation is normally given by the so-called Boussinesq's approximation, which states that the momentum transfer caused by turbulent eddies can be modelled using the concept of an eddy viscosity coefficient. Mathematically,

it is constructed using extra diffusion terms where the mixing intensity is controlled by such eddy viscosity. In the RANS approach, the eddy viscosity coefficient accounts for both 2D large scale turbulence and 3D turbulence and it is thus computed by models that consider the full structure of shallow flow turbulence. Such models range from simple zero-equation models (e.g. constant eddy viscosity model, parabolic eddy viscosity model or depth-averaged mixing length model), which assume that turbulence is dissipated where it is generated, to the more advanced eddy-viscosity models, which consider extra equations to account for the transport of turbulence (e.g. $k - \epsilon$ turbulence model) [18].

When using the RANS methodology, mean velocities are accurately predicted, however, velocity fluctuations and phenomena such as gravity waves (e.g. seiches) cannot be represented. To circumvent this limitation, the unsteady RANS (URANS) [22, 8] approach will be used in this study. The idea of using the URANS approach is motivated by the particular character of shallow water turbulence (i.e. the presence of two well-defined turbulent cascades) [3]. 2D large-scale vortices are normally resolved by means of a high-order approximation of the numerical solution, whereas 3D small-scale turbulence can be modelled by a closure equation as described before. In the literature, it is possible to find a broad variety of turbulence closure models. Some of such turbulence models only account for small-scale 3D turbulence and others also include the effect of unresolved 2D eddies. The shallow water URANS approach can be variously called: horizontal LES (H-LES), depth averaged LES (DA-LES) or DA-URANS. Nevertheless, and as stated in [22], none of these methodologies can be considered a LES model in the usual sense, as they are depth averaged and 3D turbulence always has to be modelled. For this reason, in this work we will always refer to them as DA-URANS.

Once the mathematical model is defined, an adequate numerical scheme must be selected. The turbulence modelling requires a high order approximation of the convective fluxes to avoid extra numerical diffusion and to reduce dispersion errors [23]. The non-physical diffusion at small wave numbers may damp the turbulent fluctuations to be resolved and the URANS approach may ultimately be turned into the traditional RANS approach. Apart from turbulence modelling, it has been widely reported in the literature that an accurate resolution of shallow water waves also requires a high order of accuracy [24, 25]. In this work, the design of a RANS/URANS simulation model for the SWE with bottom topography and friction, based on arbitrary order augmented WENO-ADER schemes [26], is explored. In particular, WENO-ADER schemes are applied to the computation of the convective fluxes and source terms. Alternatively, different approaches for the discretization of the diffusive terms modelling turbulent mixing are considered and assessed. Such approaches comprise a WENO-ADER reconstruction, a high order polynomial-ADER reconstruction and a second order discretization. Due to the dominant character of the convective terms in the numerical solution, the second order discretization of the diffusive terms was chosen for the sake of simplicity and computational efficiency.

The numerical scheme is explicit and integration in time is done in a single step thanks to the ADER approach. Such method successfully allows the construction of arbitrary order schemes for systems of hyperbolic conservation laws [27, 28, 29]. It is of particular interest for this work to consider the application of ADER schemes for the resolution of geophysical problems [30, 31, 25], specially for the resolution of the SWE [32, 25, 33, 34, 35, 36].

The methods are tested here up to a 3-rd order of accuracy, but they can be extended up to the desired order of accuracy provided the approximation of time derivatives has been computed by means of the Cauchy-Kowalevski (CK) procedure. This circumvents Butcher's barrier appearing for Runge-Kutta (RK) integrators [37]. Source terms are taken into account at both cell interfaces and inside cells [26, 38]. The augmented-solver approach, which ensures an exact equilibrium between fluxes and sources at cell interfaces, is adopted by using the ARoe LFS solver presented in [26]. The combination of this solver with a suitable integration of source terms inside cells makes the resulting scheme well-balanced, preserving the quiescent equilibrium. Such combination has already been used to construct high order numerical methods for the SWE with bed topography and Coriolis [38]. It must

be borne in mind that the bottom and friction source terms, present in the model herein proposed, have a different nature: the former is a geometric source term whereas the latter is non-geometric. Therefore, a different numerical treatment is required for each of them. In this work, the bottom source term is integrated using the augmented approach in [38], whereas the friction source term is only included inside cells using a traditional quadrature rule. This allows the construction of a well-balanced scheme that preserves the quiescent equilibrium with machine precision and converges with high order of accuracy to other solutions involving moving water.

The WENO reconstruction is another key feature of the numerical method herein used. It preserves the high order of accuracy in smooth regions, with low diffusion and dispersion errors [39], and is able to capture sharp gradients avoiding spurious oscillations. Furthermore, thanks to the shock-capturing character of the solvers used, the celerity of gravity waves is accurately reproduced. Seiches should be thus accurately captured.

The main advantages of using augmented WENO-ADER-type schemes are: a) the scheme can be extended up to the desired accuracy without upper bounds, allowing the computation of 2D turbulent scales [26, 40]; b) the scheme is explicit and fully discrete (i.e. it does not involve the computation of fluxes at different sub-steps like RK integrators and consequently, it is computationally more efficient [40]); c) the scheme allows the preservation of equilibrium states of relevance, in particular, the well-balanced equilibrium [38]; d) wave celerities are accurately computed, as a result of the combination of a shock-capturing solver with a high order scheme; and e) there is no need of a high mesh refinement making large computational domains affordable. Furthermore, the augmented WENO-ADER scheme considered in this work ensures convergence with mesh refinement at the prescribed rate even in presence of source terms, as shown in [26, 38].

The proposed model is herein applied to the resolution of transient problems involving resonant phenomena. In particular, we focus on the coupling between the shedding of vortices and standing gravity waves (i.e. seiches) in open channels with lateral cavities. The methods are validated using experimental data measured in a) a channel with a single cavity [8] and b) channels with multiple lateral cavities [9, 41]. A longitudinal seiche appears for case a) while a transverse seiche appears for case b). The experimental data used as a benchmark include both velocities and water depths. Thanks to the URANS approach the temporal fluctuations of the 2D vortical structures are accurately reproduced: the experimental seiching frequency is reproduced with an error lower than a 6% in all cases. On the contrary, the RANS approach proved not to be suitable for modelling resonant flows: the large amount of dissipation provided by such technique smooths artificially the flow surface oscillations leading to nonphysical results.

2. The mathematical model

2.1. System definition

The SWE are based on a 2D depth-averaged and hydrostatic model suitable for free-surface flows where the vertical dimension is much smaller than the longitudinal dimensions. The SWE are composed by the equation for the conservation of mass and momentum and are written in matrix form as follows:

$$\frac{\partial \mathbf{U}}{\partial t} + \frac{\partial \mathbf{F}(\mathbf{U})}{\partial x} + \frac{\partial \mathbf{G}(\mathbf{U})}{\partial y} = \mathbf{S} + \mathbf{D}, \tag{1}$$

where x and y stand for the Cartesian coordinates, t is the time, $\mathbf{U} = \mathbf{U}(x, y, t) \in \mathcal{C} \subset \mathbb{R}^3$ is the vector of conserved quantities that takes values on $\mathcal{C}$:

$$\mathbf{U} = \begin{pmatrix} h \\ hu \\ hv \end{pmatrix}, \tag{2}$$

4

$\mathbf{F} = \mathbf{F}(\mathbf{U}) : \mathcal{C} \longrightarrow \mathbb{R}^3$ and $\mathbf{G} = \mathbf{G}(\mathbf{U}) : \mathcal{C} \longrightarrow \mathbb{R}^3$ are the physical fluxes on the coordinate directions x and y, respectively:

$$\mathbf{F} = \begin{pmatrix} hu \\ hu^2 + \frac{1}{2}gh^2 \\ huv \end{pmatrix}, \quad \mathbf{G} = \begin{pmatrix} hv \\ hvu \\ hv^2 + \frac{1}{2}gh^2 \end{pmatrix} \tag{3}$$

and the vectors $\mathbf{S}$ and $\mathbf{D}$ stand for the source and diffusion terms, which will be detailed below. Note that g is the acceleration of gravity, h is the water depth, hu is the depth averaged unitary discharge in the x direction and hv the depth averaged unitary discharge in the y direction.

The methods herein described are based on the assumption that the convective part of the system in Equation (1) is hyperbolic. The system in Equation (1) is said to be *hyperbolic* if the matrix $\mathcal{J}(\mathbf{U}, \mathbf{n}) \in \mathbb{R}^{3 \times 3}$ defined as:

$$\mathcal{J}(\mathbf{U}, \mathbf{n}) = \frac{\partial \mathbf{F}}{\partial \mathbf{U}} n_x + \frac{\partial \mathbf{G}}{\partial \mathbf{U}} n_y, \tag{4}$$

is diagonalizable with real eigenvalues for all $\mathbf{n} = (n_x, n_y) \in \mathbb{R}^2$ and for all $\mathbf{U} \in C$ with $C \subseteq \mathbb{R}^3$ the subset of physically relevant values of $\mathbf{U}$. If all the eigenvalues are distinct, then the system is said to be *strictly hyperbolic* [42].

The longitudinal and transversal velocities, u and v are depth-averaged mean components in the term of the definition of the Reynolds decomposition. The water depth h also corresponds to a mean value. The Reynolds decomposition of the instantaneous values of depth averaged velocities and water depth, hereafter denoted as U, V, and H respectively, reads:

$$U(x, y, t) = u(x, y, t) + u'(x, y, t) \qquad V(x, y, t) = v(x, y, t) + v'(x, y, t) \tag{5}$$

$$H(x, y, t) = h(x, y, t) + h'(x, y, t) \tag{6}$$

Mean values may be obtained by several types of averaging depending on the nature of the flow [43]. The symbol $(')$ denotes turbulent fluctuation of the depth averaged values around its mean. In general, the mean values are time dependent, only under steady conditions they do not depend on time. The methods herein proposed aim at the resolution of the evolution in time of the mean properties governed by (1)–(2). The fluctuating terms are not directly resolved, though their effect in the transport of mean quantities is incorporated in the equations by means of a turbulence model.

The term $\mathbf{S} = \mathbf{S_z} + \mathbf{S_f}$ includes the source terms, which involve the stress exerted by the bottom topography, $\mathbf{S_z}$, and by the bed roughness, $\mathbf{S_f}$. Such sources are also called bed slope and friction source terms respectively and are written as:

$$\mathbf{S_z} = \begin{pmatrix} 0 \\ -gh\frac{dz}{dx} \\ -gh\frac{dz}{dy} \end{pmatrix}, \quad \mathbf{S_f} = \begin{pmatrix} 0 \\ -c_f |\mathbf{v}| u \\ -c_f |\mathbf{v}| v \end{pmatrix}, \tag{7}$$

where $|\mathbf{v}| = \sqrt{u^2 + v^2}$ is the velocity magnitude, $z = z(x, y)$ represents the bottom topography, which is fixed in time, and c_f is the friction coefficient, computed using Manning's formulation as follows:

$$c_f = \frac{gn^2}{h^{1/3}}. \tag{8}$$

On the other hand, the term $\mathbf{D}$ includes the molecular and the turbulent diffusion, being the latter a model of the mixing processes happening at the small turbulent scales according to the RANS and

5

URANS approach. The vector $\mathbf{D}$ is thus expressed as the sum of the molecular and the turbulent diffusion:

$$\mathbf{D} = \begin{pmatrix} 0 \\ \left[\frac{\partial}{\partial x} \left(\nu h \frac{\partial u}{\partial x} \right) + \frac{\partial}{\partial y} \left(\nu h \frac{\partial u}{\partial y} \right) \right] + \left[-\frac{\partial h \overline{u'u'}}{\partial x} - \frac{\partial h \overline{u'v'}}{\partial y} \right] \\ \left[\frac{\partial}{\partial x} \left(\nu h \frac{\partial v}{\partial x} \right) + \frac{\partial}{\partial y} \left(\nu h \frac{\partial v}{\partial y} \right) \right] + \left[-\frac{\partial h \overline{v'u'}}{\partial x} - \frac{\partial h \overline{v'v'}}{\partial y} \right] \end{pmatrix}, \tag{9}$$

where ν is the dynamic viscosity of the fluid and $\overline{u'u'}$, $\overline{u'v'}$, $\overline{v'u'}$ and $\overline{v'v'}$ are the depth-averaged Reynolds turbulent stresses, which can be approximated by means of Boussinesq's assumption. Note that the overline denotes mean values of the fluctuations. This assumption states that the momentum transfer caused by turbulent eddies can be modelled using the concept of an eddy viscosity. The Reynolds stress tensor is thus proportional to the mean strain rate tensor. Following [8, 21], the following approximations are used:

$$-\overline{u'u'} = 2\nu_t \frac{\partial u}{\partial x} - \frac{2}{3}k \tag{10}$$

$$-\overline{u'v'} = -\overline{v'u'} = \nu_t \left(\frac{\partial u}{\partial y} + \frac{\partial v}{\partial x} \right) \tag{11}$$

$$-\overline{v'v'} = 2\nu_t \frac{\partial v}{\partial y} - \frac{2}{3}k \tag{12}$$

where k is the mean and depth averaged turbulent kinetic energy, defined as $k = \frac{1}{2}(\overline{u'}^2 + \overline{v'}^2)$. Different formulations of the viscous and turbulent diffusion terms in (9) are found in the literature [19, 8, 20, 21]. In this work, we consider the approach provided in [20, 21, 17], where the diffusion terms are expressed as $\mathbf{D} = \mathbf{D_x} + \mathbf{D_y}$, where:

$$\mathbf{D_x} = \frac{\partial}{\partial x} \begin{pmatrix} 0 \\ h T_{xx} \\ h T_{yx} \end{pmatrix}, \quad \mathbf{D_y} = \frac{\partial}{\partial y} \begin{pmatrix} 0 \\ h T_{xy} \\ h T_{yy} \end{pmatrix}, \tag{13}$$

with T_{xx}, T_{xy}, T_{yx} and T_{yy} the depth-averaged stresses, which read as in [21]:

$$T_{xx} = 2(\nu + \nu_t)\frac{\partial u}{\partial x} \tag{14}$$

$$T_{xy} = T_{yx} = (\nu + \nu_t)\left(\frac{\partial u}{\partial y} + \frac{\partial v}{\partial x} \right) \tag{15}$$

$$T_{yy} = 2(\nu + \nu_t)\frac{\partial v}{\partial y} \tag{16}$$

where ν is the fluid viscosity and ν_t the turbulent (eddy) viscosity. Note that k in (10)–(12) will be neglected as a zero-equation model for ν_t will be used [21].

2.2. Turbulence models for the eddy viscosity ν_t

3D and 2D turbulent structures coexist in shallow water flows and it corresponds to a spectral distribution of energy as displayed in Figure 1. Both 3D and 2D vortical structures participate in the mass and momentum exchange within the flow. However, the nature of each vortical movement is different. 3D turbulence is mainly produced by the friction with the solid boundaries and comprises length scales smaller than the water depth. 2D turbulence is generated by gradients of horizontal shear stress due to gradients of the velocity field between flow regions. The length scales are typically larger than the water depth [22, 3].

The most common techniques to solve shallow water flows using a 2D model are based on the URANS and RANS approaches. The range of scales resolved (i.e. computed with the set of equations listed in the mathematical model) or modelled (i.e. computed by means of a closure equation) when using such methods is depicted in Figure 1. The URANS approach usually resolves the large scale motions of the flow (2D horizontal eddies) that contribute most to the turbulent transport but requires a model for the unresolved small scale turbulent processes (3D turbulence) that involve vertical mixing. The depth-averaged parabolic eddy viscosity model is one of the most preferred models to represent the small scale turbulence produced by the friction with the bottom [3]. On the other hand, the RANS approach does not resolve any turbulent scale. The 2D large scale turbulent mixing and the 3D small scale turbulent dissipation are thus modelled. The depth-averaged mixing length model is often used as the closure equation. The depth-averaged mixing length model will be hereafter considered for both RANS and URANS simulation, as it allows to model the unresolved 2D small eddies (if necessary when the resolution is not enough) and the 3D unresolved turbulent motion.

From the point of view of a URANS model applied to shallow water flows, the large scale 2D horizontal eddies are incorporated and considered as part of a time varying mean flow (i.e. $u(x, y, t)$, $v(x, y, t)$ and $h(x, y, t)$). From the point of view of a RANS model, all the time varying components are modelled, hence the mean fields corresponds to the time-averaged variables (i.e. $u(x, y)$, $v(x, y)$ and $h(x, y)$).
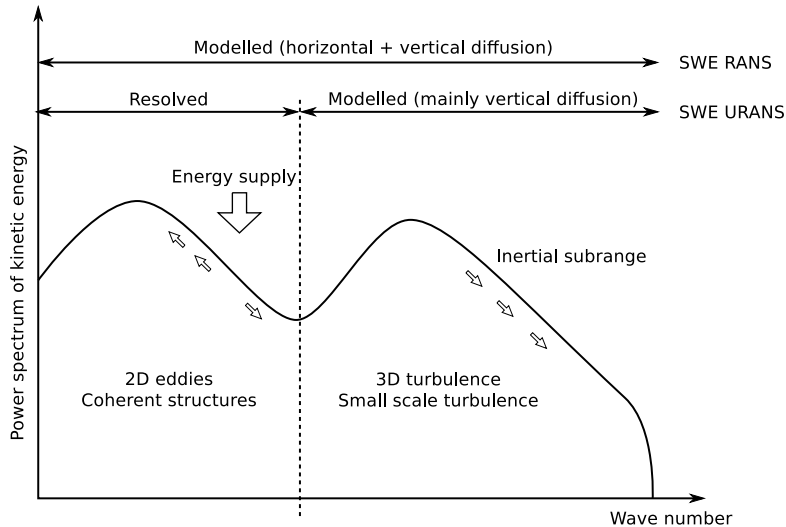

Figure 1: Schematic representation of the two-range turbulence spectrum in shallow water flows. The wave number is defined as the inverse turbulent length, which is related with the size of the eddies. The range of scales modelled/resolved by the URANS and RANS approaches is provided. This figure is adapted from [22, 3].

2.3. Depth-averaged mixing length model

The depth-averaged mixing length model is used to account for both the horizontal (2D) and vertical production of turbulence (3D). This model reads as:

$$\nu_t = \sqrt{(\nu_t^v)^2 + (\nu_t^h)^2} \tag{17}$$

where ν_t^v and ν_t^h are the vertical and horizontal eddy viscosities. The vertical component is mainly produced due to the bed friction and it is calculated as:

$$\nu_t^v = \lambda U^* h \,, \tag{18}$$

where λ is an empirical coefficient and $U^* = \sqrt{c_f(u^2 + v^2)}$ is the bed shear velocity. Note that c_f is the friction coefficient defined in Equation (8). The parameter λ can be theoretically estimated as $\kappa/6$, with κ the Von Karman's constant, though it is normally retained as a calibration parameter [21]. The model in Equation (18) corresponds to the depth-averaged parabolic eddy viscosity model.

On the other hand, the horizontal component of turbulence is mainly produced by horizontal velocity gradients and it is resolved as:

$$\nu_t^h = \beta l_s^2 \sqrt{2\left(\frac{\partial u}{\partial x}\right)^2 + 2\left(\frac{\partial v}{\partial y}\right)^2 + \left(\frac{\partial u}{\partial y} + \frac{\partial v}{\partial x}\right)^2} \tag{19}$$

with $l_s = \kappa \, min(c_m h, y_w)$ [21, 19], where c_m is an empirical coefficient (normally set to 0.267 [19]), y_w is the distance to the nearest wall and β is a calibration constant.

In this work, the depth-averaged mixing length model is used both for URANS and RANS simulations (see Figure 1). In the case of URANS approach, the horizontal eddies are mostly resolved. The strength of the horizontal turbulent mixing, β, is thus much lower than in the case of RANS simulations. This yields to an eddy viscosity coefficient that is mainly composed by the vertical diffusivity. Note that in the limit when $\beta = 0$, the depth-averaged parabolic eddy viscosity model is recovered (i.e. only the vertical diffusivity is modelled). On the other hand, when adopting the RANS methodology, the horizontal diffusivity may become dominant, specially in cases involving strong shearing flows. In such cases, the mixing processes are not represented as convective processes (as it is done with URANS simulation) but as purely diffusive processes, governed by ν_t.

It is worth pointing out that the use of the eddy viscosity in (19) for URANS simulation, in combination with the approximation of the depth-averaged Reynolds stress tensor in (14)–(16), is equivalent to the well-known Smagorinsky (SGS) sub-grid model when the coefficient βl_s^2 is of the order of magnitude of $C_s \Delta x$, where C_s is found in the interval 0.4 to 0.8 for shallow flows [44, 45]. This evidences the role of the horizontal component of the eddy viscosity in (19) as a sub-grid dissipation model for the unresolved scales.

3. Numerical model: augmented WENO-ADER scheme in Cartesian grid

Let us consider the system of conservation laws in (1)–(2) to compose the following Initial Boundary Value Problem (IBVP):

$$\begin{cases} \text{PDEs:} & \dfrac{\partial \mathbf{U}}{\partial t} + \nabla \cdot (\mathbf{F}, \mathbf{G}) = \mathbf{S} + \mathbf{D} \\[2ex] \text{IC:} & \mathbf{U}(\mathbf{x}, 0) = \mathring{\mathbf{U}}(\mathbf{x}) \quad \forall \mathbf{x} \in \Omega \\[2ex] \text{BC:} & \mathbf{U}(\mathbf{x}, t) = \mathbf{U}_{\partial\Omega}(\mathbf{x}, t) \quad \forall \mathbf{x} \in \partial\Omega \end{cases} \tag{20}$$

8

defined in the domain $\Omega \times [0, T]$, where $\Omega = [a, b] \times [c, d]$ is the spatial domain. The initial condition is given by $\overset{\circ}{\mathbf{U}}(\mathbf{x})$ and the boundary condition by $\mathbf{U}_{\partial\Omega}(\mathbf{x}, t)$. The spatial domain is discretized in $N_x \times N_y$ volume cells, defined as $\Omega_{ij} \subseteq \Omega$, such that $\Omega = \bigcup_{i,j=1}^{N} \Omega_{ij}$, with cell edges at:

$$a = x_{\frac{1}{2}} < x_{\frac{3}{2}} < ... < x_{N_x-\frac{1}{2}} < x_{N_x+\frac{1}{2}} = b, \tag{21}$$

and

$$c = y_{\frac{1}{2}} < y_{\frac{3}{2}} < ... < y_{N_y-\frac{1}{2}} < y_{N_y+\frac{1}{2}} = d, \tag{22}$$

Cells and cell sizes are defined as:

$$\Omega_{ij} = \left[x_{i-\frac{1}{2}}, x_{i+\frac{1}{2}}\right] \times \left[y_{j-\frac{1}{2}}, y_{j+\frac{1}{2}}\right], \qquad i = 1, ..., N_x, j = 1, ..., N_y \tag{23}$$

and

$$\vartheta_{ij} = (x_{i+\frac{1}{2}} - x_{i-\frac{1}{2}}) \cdot (y_{j+\frac{1}{2}} - y_{j-\frac{1}{2}}), \qquad i = 1, ..., N_x, j = 1, ..., N_y, \tag{24}$$

respectively. In the case of regular grid we have $\vartheta_{ij} = \Delta x^2$.

Inside each cell, at time t^n, the conserved quantities are defined as cell averages as:

$$\overline{\mathbf{U}}_{ij}^n = \frac{1}{\vartheta_{ij}} \int_{\Omega_{ij}} \mathbf{U}(\mathbf{x}, t^n) dA \qquad i = 1, ..., N_x, j = 1, ..., N_y. \tag{25}$$

where $dA = dxdy$ is the differential element of surface. Let us consider again the system in (20) and integrate it over the discrete domain $\Omega_{ij} \times \Delta t$, where $\Delta t = t^{n+1} - t^n$. Application of the Gauss-Ostrogradsky theorem yields to:

$$\overline{\mathbf{U}}_{ij}^{n+1} = \overline{\mathbf{U}}_{ij}^n - \frac{1}{\vartheta_{ij}} \int_0^{\Delta t} \int_{\partial\Omega_{ij}} (\mathbf{F}, \mathbf{G}) \cdot \hat{\mathbf{n}} dl dt + \frac{1}{\vartheta_{ij}} \int_0^{\Delta t} \int_{\Omega_{ij}} \mathbf{S} \, dA dt + \frac{1}{\vartheta_{ij}} \int_0^{\Delta t} \int_{\Omega_{ij}} \mathbf{D} \, dA dt, \tag{26}$$

where dl is the differential length. If we consider a regular Cartesian grid with $\Delta x = \Delta y$, we obtain the following fully-discrete updating formula:

$$\overline{\mathbf{U}}_{ij}^{n+1} = \overline{\mathbf{U}}_{ij}^n - \frac{\Delta t}{\Delta x^2} \left(\mathbf{F}_{i+1/2,j}^- - \mathbf{F}_{i-1/2,j}^+\right) - \frac{\Delta t}{\Delta x^2} \left(\mathbf{G}_{i,j+1/2}^- - \mathbf{G}_{i,j-1/2}^+\right) + \frac{\Delta t}{\Delta x^2} \left(\bar{\mathbf{S}}_{ij} + \bar{\mathbf{D}}_{ij}\right), \tag{27}$$

where $\mathbf{F}_{i\mp1/2,j}^\pm$ and $\mathbf{G}_{i,j\mp1/2}^\pm$ are the numerical fluxes at cell interfaces and

$$\bar{\mathbf{S}}_{ij} \approx \frac{1}{\Delta t} \int_0^{\Delta t} \int_{x_{i-1/2}}^{x_{i+1/2}} \int_{y_{j-1/2}}^{y_{j+1/2}} \mathbf{S} \, dy dx \, d\tau, \quad \bar{\mathbf{D}}_{ij} \approx \frac{1}{\Delta t} \int_0^{\Delta t} \int_{x_{i-1/2}}^{x_{i+1/2}} \int_{y_{j-1/2}}^{y_{j+1/2}} \mathbf{D} \, dy dx \, d\tau. \tag{28}$$

are the approximation of the space-time integral of the source terms and diffusion terms inside the cell. Both approximations are explicit. The time step, Δt, is computed dynamically according to the condition in [46] to preserve the stability of the numerical solution. Such condition states that the sum of the Courant-Friedrichs-Levy (CFL) and Peclet (Pe) number must be below 0.5 for Cartesian meshes.

The numerical fluxes are computed as the space-time integral of the numerical fluxes over the cell edges. To construct a numerical scheme of order $(2k-1)$-th, it is sufficient to approximate such integrals using a $(2k-1)$-th order Gaussian quadrature, thus requiring k quadrature points. For instance, the numerical flux $\mathbf{F}_{i+1/2,j}^-$ is computed as follows:

$$\mathbf{F}^-_{i+1/2,j} = \frac{\Delta x}{2} \sum_{q=1}^{k} w_q \mathbf{F}^-_{i+1/2,j,q} \tag{29}$$

where w_q are the Gaussian weights inside the interval $[-1,1]$ at the $q = 1,...,k$ quadrature points along the cell edge and $\mathbf{F}^-_{i+1/2,j,q}$ the numerical fluxes at each of these points, computed by means of the resolution of the Cauchy problem.

The numerical fluxes are computed solving an arbitrary order approximation of the Cauchy problem at the quadrature points along cell interfaces. This is given by the so-called DRP, which is defined in the x direction for the numerical fluxes on the east and west interfaces and in the y direction for those fluxes on the north and south interfaces. It is worth noting that the source term is included in the definition of the DRP, according to [26]. The DRP_K defined in the x direction, at the interface $i+1/2$ and quadrature point q, reads as [26]:

$$\begin{cases} \dfrac{\partial \mathbf{U}}{\partial t} + \dfrac{\partial \mathbf{F}(\mathbf{U})}{\partial x} = \bar{\mathbf{S}}_{i+1/2} \\[4mm] \mathbf{U}(x, t=0) = \begin{cases} \mathbf{U}_{ij}(x, y_{i+1/2,j,q}) & x < 0 \\ \mathbf{U}_{i+1\,j}(x, y_{i+1/2,j,q}) & x > 0 \end{cases} \end{cases} \tag{30}$$

where $\mathbf{U}_{ij}(x,y)$ and $\mathbf{U}_{i+1\,j}(x,y)$ are smooth spatial reconstructions, defined using the WENO method. Such functions are evaluated at the particular location where the DRP is defined, $y = y_{i+1/2,j,q}$. On the other hand, $\bar{\mathbf{S}}_{i+1/2}$ represents the integral of the source term at cell interfaces, which only is non-zero when considering geometric source terms (e.g. bed elevation source term). It is computed as:

$$\bar{\mathbf{S}}_{i+1/2} \approx \frac{1}{\Delta t} \int_0^{\Delta t} \int_{x^-_{i+1/2}}^{x^+_{i+1/2}} \mathbf{S} \, dx \, d\tau \,. \tag{31}$$

The solution for the DRP in (30) is constructed using the flux expansion approach as:

$$\begin{aligned} \mathbf{F}^-_{i+1/2,j,q} &= \mathbf{F}^{-,(0)}_{i+1/2,j,q} + \sum_{k=1}^{K} \mathbf{F}^{-,(k)}_{i+1/2,j,q} \frac{\Delta t^k}{(k+1)!} \,, \\[3mm] \mathbf{F}^+_{i+1/2,j,q} &= \mathbf{F}^{+,(0)}_{i+1/2,j,q} + \sum_{k=1}^{K} \mathbf{F}^{+,(k)}_{i+1/2,j,q} \frac{\Delta t^k}{(k+1)!} \,, \end{aligned} \tag{32}$$

where $\mathbf{F}^{-,(0)}_{i+1/2,j,q}$, $\mathbf{F}^{-,(k)}_{i+1/2,j,q}$, $\mathbf{F}^{+,(0)}_{i+1/2,j,q}$ and $\mathbf{F}^{+,(k)}_{i+1/2,j,q}$ are computed by solving the DRP_K. When using the LFS-ARoe solver [26], the coefficients of (32) read as:

$$\begin{aligned} \mathbf{F}^{-,(k)}_{i+1/2} &= \mathbf{F}^{(k)}_{i_E} + \sum_{m=1}^{N_\lambda} \left(\widetilde{\lambda}^- \alpha^{(k)} - \beta^{-,(k)} \right)^m_{i+1/2} \widetilde{\mathbf{e}}^m_{i+1/2}, \quad k = 0, K \\[3mm] \mathbf{F}^{+,(k)}_{i+1/2} &= \mathbf{F}^{(k)}_{(i+1)_W} + \sum_{m=1}^{N_\lambda} \left(\widetilde{\lambda}^+ \alpha^{(k)} - \beta^{+,(k)} \right)^m_{i+1/2} \widetilde{\mathbf{e}}^m_{i+1/2}, \quad k = 0, K \end{aligned} \tag{33}$$

where $\mathbf{F}^{(k)}_{i_E}$ and $\mathbf{F}^{(k)}_{(i+1)_W}$ are the left and right-hand limits to the cell edge of the physical flux ($k = 0$) and their k-th time derivatives, $\alpha^{(k)}$ are the wave strengths, $\beta^{-,(k)}$ the source strengths and $\widetilde{\lambda}^\pm$ and $\widetilde{\mathbf{e}}^m_{i+1/2}$ the approximate wave celerities and eigenvectors defined using Roe's averages [47]. The computation of the aforementioned quantities is detailed in [38]. The fluxes $\mathbf{G}^-_{i,j+1/2,q}$ and $\mathbf{G}^+_{i,j-1/2,q}$, are computed analogously.

3.1. Equilibrium properties

When the velocity vanishes, the equation for the conservation of energy and momentum yield to:

$$\nabla (h + z) = 0 \tag{34}$$

which represents the hydrostatic equilibrium, also known in the literature as *lake at rest* condition. At the discrete level and considering a Cartesian grid, Equation (34) is decomposed into the Cartesian directions as:

$$\delta (h + z)_{x_2, x_1} = 0, \qquad \delta (h + z)_{y_2, y_1} = 0 \tag{35}$$

where (x_1, y_1) and (x_2, y_2) are two different points. To construct a well-balanced scheme, the previous discrete conditions in (35) must be satisfied. This can only be achieved if the WENO reconstruction method is applied to $\eta = h + z$ and z first, and h is computed from the difference of these reconstructions as $h_{(\cdot)}^{(0)} = \eta_{(\cdot)}^{(0)} - z_{(\cdot)}^{(0)}$, where $\eta_{(\cdot)}^{(0)}$ and $z_{(\cdot)}^{(0)}$ are the reconstructed water surface elevation and bottom elevation and $h_{(\cdot)}^{(0)}$ the computed water depth. The discharges hu and hv are also reconstructed using the WENO method.

3.2. Numerical approximation of source terms

Apart from a suitable reconstruction procedure, source terms have to be properly integrated both at cell interfaces, using the discretization in (28), and inside cells, using (31), to construct a well balanced scheme. The numerical approximation of source terms in (28) and (31) can be expressed using a Taylor power series expansion as follows:

$$\bar{\mathbf{S}}_{ij} = \bar{\mathbf{S}}_{ij}^{(0)} + \sum_{k=1}^{K} \bar{\mathbf{S}}_{ij}^{(k)} \frac{\Delta t^k}{(k+1)!}, \qquad \bar{\mathbf{S}}_{i+1/2} = \bar{\mathbf{S}}_{i+1/2}^{(0)} + \sum_{k=1}^{K} \bar{\mathbf{S}}_{i+1/2}^{(k)} \frac{\Delta t^k}{(k+1)!}, \tag{36}$$

where

$$\bar{\mathbf{S}}_{ij}^{(0)} = \int_{x_{i-1/2}}^{x_{i+1/2}} \int_{y_{j-1/2}}^{y_{j+1/2}} \mathbf{S}_i(x, y, 0) \, dy dx, \qquad \bar{\mathbf{S}}_{i+1/2}^{(0)} = \int_{x_{i+1/2}^-}^{x_{i+1/2}^+} \mathbf{S}_i(x, y, 0) \, dx,$$

$$\bar{\mathbf{S}}_{ij}^{(k)} = \int_{x_{i-1/2}}^{x_{i+1/2}} \int_{y_{j-1/2}}^{y_{j+1/2}} \partial_t^k \mathbf{S}(x, y, 0) \, dy dx, \qquad \bar{\mathbf{S}}_{i+1/2}^{(k)} = \int_{x_{i+1/2}^-}^{x_{i+1/2}^+} \partial_t^k \mathbf{S}(x, y, 0) \, dx, \tag{37}$$

are the spatial integrals of the source term and its time derivatives at the initial time.

It must be noted that the first component of the source term vector will always be zero, as no source is considered for the mass conservation equation. On the other hand, the source term may be non-zero for the x and y momentum equations. The 2-nd and 3-rd components of the numerical source term, $\bar{\mathbf{S}}_{ij}$, corresponding to the x and y momentum equations, will be hereafter referred to as $\bar{S}_{ij}^x$ and $\bar{S}_{ij}^y$, respectively. The same notation is used for $\bar{\mathbf{S}}_{i+1/2}$.

3.2.1. Bed slope

Bed slope source term must be discretized in a particular way so that the scheme preserves the well-balanced property. Since this source has a geometric nature, it is discretized both at cell interfaces and inside cells. At cell interfaces, the leading term is computed as:

$$\bar{S}_{i+1/2}^{x,(0)} = \left(-g\bar{h}\delta z\right)_{i+1/2}^{(0)}, \qquad \bar{S}_{i+1/2}^{y,(0)} = 0, \tag{38}$$

which satisfy the steady state equilibrium condition $\left(\widetilde{\lambda}^{\pm} \alpha^{(0)} - \beta^{\pm,(0)} \right)_{i+1/2}^{m} = 0$ in Equation (33). Note that $\bar{h}_{i+1/2}^{(0)} = 0.5(h_{i_E}^{(0)} + h_{(i+1)_W}^{(0)})$ and $\delta z_{i+1/2}^{(0)} = z_{(i+1)_W}^{(0)} - z_{i_E}^{(0)}$.

Higher order terms are computed as:

$$\bar{\mathbf{S}}_{i+1/2}^{x,(k)} = \left(-g\bar{h}^{(k)} \delta z^{(0)} \right)_{i+1/2} . \tag{39}$$

The cell-centered discretization of the bed slope source term needs to be derived to also retain the order of accuracy of the scheme. To this end, the approach proposed in [38], based on Romberg's integration, is used for the zero-th order terms:

$$\bar{S}_{ij}^{x,(0)} = \frac{\Delta x}{2} \sum_{\beta=1}^{k} w_{\beta} \left\{ \bar{S}_{ij,\beta}^{x,(0)} \right\}_{m}^{n} , \qquad \bar{S}_{ij}^{y,(0)} = \frac{\Delta x}{2} \sum_{\alpha=1}^{k} w_{\alpha} \left\{ \bar{S}_{ij,\alpha}^{y,(0)} \right\}_{m}^{n} \tag{40}$$

where $\left\{ \bar{S}_{ij,\beta}^{x,(0)} \right\}_{m}^{n}$ and $\left\{ \bar{S}_{ij,\alpha}^{y,(0)} \right\}_{m}^{n}$ are based on Richardson's extrapolation of the differential formulation of the integral of the source term [38]. Such extrapolation provides an arbitrary order approximation of the integral of the bed slope source term along the straight line connecting two quadrature points at opposite walls (in Cartesian directions).

Concerning the derivative terms, there is no need of a particular discretization to ensure the well-balanced property as time derivatives vanish under steady state. A 2D Gaussian integration is used [38]:

$$\bar{S}_{ij}^{x,(k)} = \frac{\Delta x^2}{4} \sum_{\beta=1}^{k} w_{\beta} \sum_{\alpha=1}^{k} w_{\alpha} \left(-gh^{(k)} \partial_x z \right)_{\alpha,\beta} , \qquad \bar{S}_{ij}^{y,(k)} = \frac{\Delta x^2}{4} \sum_{\beta=1}^{k} w_{\beta} \sum_{\alpha=1}^{k} w_{\alpha} \left(-gh^{(k)} \partial_y z \right)_{\alpha,\beta} \tag{41}$$

where $h_{\alpha,\beta}^{(k)}$ is the k-th time derivative of h at the quadrature point.

3.2.2. Friction

The friction term is discretized here as a centered source term, which means that it is not accounted for in the definition of the DRP. Such approach does not ensure an exact equilibrium between bed and friction slope but ensures convergence with arbitrary order to this equilibrium state. The following 2D Gaussian quadrature is proposed to approximate the integral of the leading term inside the cell:

$$\bar{S}_{ij}^{x,(0)} = \frac{\Delta x^2}{4} \sum_{\alpha=1}^{k} w_{\alpha} \sum_{\beta=1}^{k} w_{\beta} \left(-c_f \left| \mathbf{v}^{(0)} \right| u^{(0)} \right)_{\alpha,\beta} , \quad \bar{S}_{ij}^{y,(0)} = \frac{\Delta x^2}{4} \sum_{\alpha=1}^{k} w_{\alpha} \sum_{\beta=1}^{k} w_{\beta} \left(-c_f \left| \mathbf{v}^{(0)} \right| v^{(0)} \right)_{\alpha,\beta} , \tag{42}$$

with $c_f = c_f(\mathbf{U}^{(0)}, n)$ and n the Manning coefficient. To construct a Gaussian quadrature for the derivative terms of the source term, the CK procedure must be used first to provide an approximation of the time derivatives of the source at the quadrature points:

$$S_{\alpha,\beta}^{x,(k)} = \frac{\partial^k}{\partial t^k} \left(-c_f \left| \mathbf{v} \right| u \right)_{\alpha,\beta} , \qquad S_{\alpha,\beta}^{y,(k)} = \frac{\partial^k}{\partial t^k} \left(-c_f \left| \mathbf{v} \right| v \right)_{\alpha,\beta} . \tag{43}$$

Then, we can construct the 2D Gaussian quadrature as follows:

$$\bar{S}_{ij}^{x,(k)} = \frac{\Delta x^2}{4} \sum_{\alpha=1}^{k} w_{\alpha} \sum_{\beta=1}^{k} w_{\beta} S_{\alpha,\beta}^{x,(k)} , \quad \bar{S}_{ij}^{y,(k)} = \frac{\Delta x^2}{4} \sum_{\alpha=1}^{k} w_{\alpha} \sum_{\beta=1}^{k} w_{\beta} S_{\alpha,\beta}^{x,(k)} . \tag{44}$$

3.3. Numerical approximation of the diffusion terms

The diffusion terms in (13) are based on Boussinesq approximation and involve the numerical approximation of spatial gradients of the velocity. Here, two different approaches to compute such spatial gradients are tested:

- Sub-cell derivative reconstruction procedure:

  This is an arbitrary order reconstruction technique originally proposed in [48]. It is based on constructing a high order polynomial inside each cell by using as interpolating data the high order reconstructed information (provided by the WENO reconstruction or any other reconstruction method [49]) at different points inside the cell. The derivatives of such polynomial will approximate the derivatives of the variables of interest.

  The WENO method for reconstructing the sub-cell data uses a stencil selection procedure to prevent spurious oscillations and guarantees monotonicity near strong gradients or discontinuities. Such features are normally observed in boundary layers, where the relation between the physical width of the boundary layer and the cell size is crucial for an accurate reconstruction of the boundary data. In cases where the width of the boundary layer is smaller than the cell size, the local velocity gradients are interpreted by the WENO reconstruction as a discontinuity between smooth flow domains (i.e. the limiting case would be given by two regions connected by a discontinuity as presented in Appendix A). The sub-cell derivative reconstruction thus yields to nil values of spatial derivatives in the boundary layer, which it is not consistent with the real physics and ultimately it leads to an underestimation of the diffusive terms in Equation 13 (i.e. the magnitude of the turbulent mixing modelled by the diffusive terms is underestimated).

  A different possibility for reconstructing the sub-cell data consists of using a linear reconstruction by means of a classical high order polynomial. With a classical polynomial, non-linear limiters, such as those present in the WENO method, are avoided. Such way, the aforementioned physical inconsistency is partially overcome as the jump in the flow velocity is spread along a length corresponding to the cell size. This avoids the limitation of large sub-cell gradients, leading to larger diffusion at these regions. The overall performance of the non-limited sub-cell derivative reconstruction procedure is better than the WENO sub-cell derivative reconstruction procedure, even though the diffusive terms are not accurately discretized either. In the framework of very high order schemes, it would be worth exploring more sophisticated reconstruction techniques that are more consistent with the physics of the flow.

- Centered differences:

  Another possibility to compute the spatial gradients is to use centered differences, departing from cell-averaged data. This approach is second order accurate and is free from limiting techniques, hence it is adequate to approximate the diffusion terms in (13). Moreover, it has lower computational cost than the sub-cell derivative reconstruction procedure. By using this discretization, Equation (13) yields to:

  $$\bar{\mathbf{D}}_{x,ij} = \Delta x \, \delta \left(\begin{array}{c} 0 \\ \bar{h}\overline{T}_{xx} \\ \bar{h}\overline{T}_{yx} \end{array} \right)_{i-1/2,j}^{i+1/2,j} , \qquad \bar{\mathbf{D}}_{y,ij} = \Delta x \, \delta \left(\begin{array}{c} 0 \\ \bar{h}\overline{T}_{xy} \\ \bar{h}\overline{T}_{yy} \end{array} \right)_{i,j-1/2}^{i,j+1/2} . \tag{45}$$

  where:

  $$\bar{h}_{i+1/2,j} = \frac{h_{i+1,j} + h_{i,j}}{2} , \qquad \bar{h}_{i-1/2,j} = \frac{h_{i,j} + h_{i-1,j}}{2} , \tag{46}$$

13

are the average water depths at x-cell interfaces, computed using cell averages. The average water depths at y-cell interfaces are computed analogously. More generally, $(\bar{\cdot})_{i+1/2,j} = \frac{(\cdot)_{i+1,j}+(\cdot)_{i,j}}{2}$ and $(\bar{\cdot})_{i,j+1} = \frac{(\cdot)_{i,j+1}+(\cdot)_{i,j}}{2}$. The approximate stresses, $\overline{T}_{xx}$, $\overline{T}_{xy}$, $\overline{T}_{yx}$ and $\overline{T}_{yy}$, are approximated using central differences as follows:

$$\left(\overline{T}_{xx}\right)_{i+1/2,j} = 2\left(\nu + \bar{\nu}_{t_{i+1/2,j}}\right)\left(\frac{u_{i+1,j}-u_{i,j}}{\Delta x}\right), \tag{47}$$

$$\left(\overline{T}_{yx}\right)_{i+1/2,j} = \left(\nu + \bar{\nu}_{t_{i+1/2,j}}\right)\left(\frac{1}{2\Delta x}\left(\frac{u_{i+1,j+1}+u_{i,j+1}}{2} - \frac{u_{i+1,j-1}+u_{i,j-1}}{2}\right) + \frac{v_{i+1,j}-v_{i,j}}{\Delta x}\right), \tag{48}$$

$$\left(\overline{T}_{xy}\right)_{i,j+1/2} = \left(\nu + \bar{\nu}_{t_{i,j+1/2}}\right)\left(\frac{u_{i,j+1}-u_{i,j}}{\Delta x} + \frac{1}{2\Delta x}\left(\frac{v_{i+1,j+1}+v_{i+1,j}}{2} - \frac{v_{i-1,j+1}+v_{i-1,j}}{2}\right)\right), \tag{49}$$

$$\left(\overline{T}_{yy}\right)_{i,j+1/2} = 2\left(\nu + \bar{\nu}_{t_{i,j+1/2}}\right)\left(\frac{v_{i,j+1}-v_{i,j}}{\Delta x}\right). \tag{50}$$

The centered differences have a truncation error of order $\mathcal{O}(\Delta x^2)$, which is lower than that of the convective part. However, due to the particular application of the scheme that involve small diffusion coefficients, the presence of the $\mathcal{O}(\Delta x^2)$ term in the truncation error is far from limiting the higher order of accuracy of the scheme (i.e. the convective term dominates over the diffusive terms as the Peclet number [46] is several orders of magnitude lower than the CFL number).

Among the two physically consistent approaches: (i) a non-WENO polynomial and (ii) the centered derivatives, the second order centered derivatives technique is eventually chosen, as stated in the Appendix A. Although the level of accuracy is lower with the centered derivatives than with a high order polynomial reconstruction, the computational effort saved with the centered derivatives compensated such selection.

3.4. Boundary wall numerical treatment: the composite wall friction model

The friction in a 1D model of a channel is computed by means of a composite Manning coefficient, which includes the friction of the lateral walls. The Horton-Einstein equation is thus used:

$$n = \left(\frac{n_b^{3/2}b + 2n_w^{3/2}h}{b}\right)^{2/3} \tag{51}$$

where n_b is the roughness coefficient of the bed, n_w the roughness coefficient of the walls, b is the width of the channel and h the water depth. In the numerical model proposed here, a composite Manning coefficient is considered in those cells containing solid walls (i.e. the boundaries that enclose the water body). The roughness coefficient in such cells, n, is computed by accounting for the contribution of the bed plus the contribution of the walls. In the case of having solid walls along the x direction, we compute the x-Manning composite coefficient as:

$$n_x = \left(\frac{n_b^{3/2}\Delta y + n_w^{3/2}h}{\Delta y}\right)^{2/3} \tag{52}$$

14

and analogously when having solid walls along the y direction:

$$n_y = \left(\frac{n_b^{3/2} \Delta x + n_w^{3/2} h}{\Delta x} \right)^{2/3} \tag{53}$$

The proposed model accounts for the shear stress on the walls by including an extra friction component on the boundary cells, introducing all the extra friction on the first row of cells by re-calculating the Manning coefficient using the Einstein-Horton formulation. The shear momentum introduced in the first cell by the effect of the wall roughness is eventually transferred to the inner cells (in the spanwise direction, towards the center of the channel) thanks to the diffusion terms and the numerical diffusion. The size of the boundary layer developed in the numerical solution will thus depend on the wall roughness, the diffusion coefficient and ultimately, in some extent, on the mesh resolution.

In the present model there is still a broken link between the wall roughness and the mixing length: both play an important role on the vortical dynamics. As a future work, it will be useful to carry out a further investigation on more accurate wall friction models by including the relation between such quantities: the wall roughness and the mixing length. For instance, it will be valuable to implement a wall friction law which could dynamically span over a certain number of cells and ultimately, develop a velocity profile over the wall. The wall roughness could thus actively participate in the vortical production of the mixing layer.

4. Numerical results

4.1. Single lateral cavities

4.1.1. Problem configuration

The fundamental behavior of unsteady flow in an open channel with a lateral cavity was investigated, both experimentally and numerically, by Kimura and Hosoda in [8]. A schematic diagram of the flow domain is shown in Figure 2. A rectangular dead zone of variable longitudinal length (two cases are proposed with $L = 15$ and $L = 22.5$ cm) is attached to the side wall of an open channel. The length in the transverse direction, W, is 15.0 cm, and the channel width, B, is 10.0 cm. The hydraulic variables for the two laboratory tests proposed in [8], hereafter referred to as Case 1 and Case 2, are listed in Table 1. For the velocity measurements, an anemometer with a propeller with a diameter of 3 mm was used for velocities over 6 cm/s, and a thermal type anemometer with a diameter of 3 mm was used for velocities below 6 cm/s. Temporal velocity variations were measured at half the depth along the interface along the $T - T'$ section in 2. One of the fundamental properties of this type of flow is the generation of seiches due to the coupling between the shedding of vortices at the opening of the cavity with a traveling gravity wave inside the cavity. A selective amplification of vortices is induced by the presence of the seiche. Such vortices are eventually transported inside the cavity and dissipated. According to [8], the analytical estimation of the period of the seiche is given by:

$$T = \frac{2L}{nc}, \quad n = 1, 2, 3, \ldots \tag{54}$$

yielding a period of $T = 0.958$ s and $T = 1.011$ s for cases 1 and 2 respectively, which are larger than the experimental measurements, in Table 1. Note that such values are estimated considering the first harmonic, that is $n = 1$.

The experiments were simulated using the proposed WENO-ADER scheme. Note that the lengths L_{up} and L_{down} in Figure 2 are required to define the computational domain. Such parameters are unspecified in the original work [8] and here we choose $L_{up} = 15$ cm and $L_{down} = 20$ cm for Case
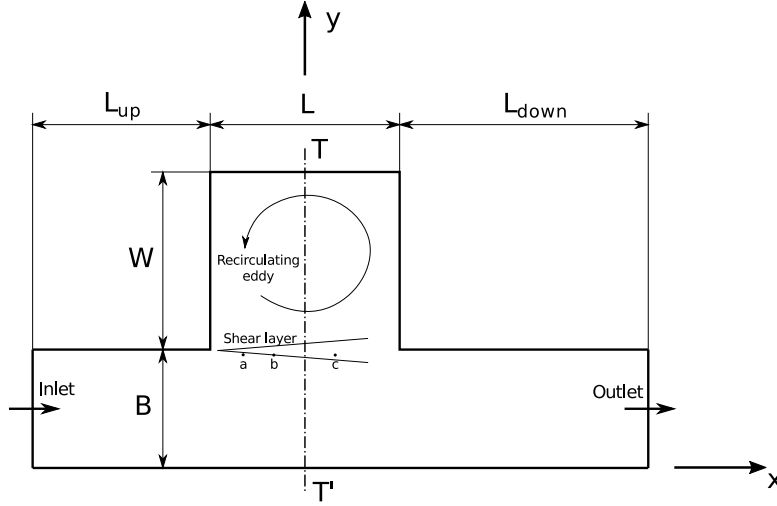
15

Figure 2: Sketch of the experimental setup used by [8] and detail of the main features of the flow.

Case	L (cm)	W (cm)	B (cm)	q (l/s)	h_0 (cm)	Slope	Fr	Re	T exp. (s)
1	15.0	15.0	10.0	0.255	1.00	1/500	0.81	2781	0.89
2	22.5	15	10.0	0.747	2.02	1/500	0.83	8150	0.87

Table 1: Experimental hydraulic parameters.

1 and $L_{up} = 15$ cm and $L_{down} = 25$ cm for Case 2. For all simulations, a stability condition of $CFL + Pe = 0.4$ is used.

4.1.2. Case 1

Numerical results for case 1 are presented in this section. Different sub-cases, defined by different calibration and simulation parameters, are presented. Details of the parameters for the simulations are summarized in Table 2. Runs 1 to 5 correspond to unsteady RANS (URANS) simulations whereas run 6 corresponds to a RANS simulation, which only resolves averaged quantities.

Run	Model	q_{bc} (l/s)	h_{bc} (cm)	ν (m^2/s)	λ	β	n_b	n_w	Δx (mm)	Order
1.1	URANS	0.255	1.0	1E-6	0.3	0.3	0.010	0.03	1.25	3
1.2	URANS	0.255	1.0	1E-6	0.3	0.3	0.010	0.03	2.5	3
1.3	URANS	0.255	1.0	1E-6	0.3	0.3	0.010	0.03	5	3
1.4	URANS	0.255	1.0	1E-6	0.3	0.3	0.010	0.03	2.5	1
1.5	URANS	0.255	1.0	1E-6	0.15	0.05	0.010	0.025	1.25	3
1.6	RANS	0.255	1.0	1E-6	1.5	2.0	0.010	0.025	1.25	1

Table 2: Numerical parameters for the turbulent model and the simulations.

The Manning coefficient has to be properly calibrated to ensure uniform flow along the channel with a water depth of $h = 1$ cm. We have selected $n_b = 0.010$ as the optimal Manning coefficient. In the original work by Kimura and Hosoda in [8], non-slip boundary conditions were imposed in combination with an adaptive mesh refinement near the walls. In this work, we consider the composite Horton-Einsten Manning formulation to account for the friction with the walls as described before. The numerical results evidence that the lower the wall roughness, the larger the velocity in the recirculation

inside the lateral cavity. According to the results, the optimal choice for the wall Manning coefficient should be between $n_w = 0.02$ and $n_w = 0.03$. A sensitivity analysis of the solution to the grid size was carried out in runs 1.1–1.3, where three different grids with $\Delta x = 1.25$ (run 1.1), $\Delta x = 2.5$ (run 1.2) and $\Delta x = 5$ mm (run 1.3) were used.

Numerical results for the time-averaged streamwise velocities along the section $T - T'$ are presented in Figure 3 (a) and results for the mean water surface evolution in time at the upstream edge of the cavity are presented in Figure 3 (b). The amplitude of the seiche decreases as the grid size increases. In addition, its period is practically not modified, as reported in [8]. It is observed that the grid resolution of $\Delta x = 5$ mm is not enough to properly capture the expected amplitude of the seiche and the measured magnitudes of velocity. On the other hand, grid sizes $\Delta x = 2.5$ and $\Delta x = 1.25$ mm provide similar results that mimic the experimental measurements and the results in [8], which means that $\Delta x = 2.5$ m is sufficient to provide the neccesary accuracy.
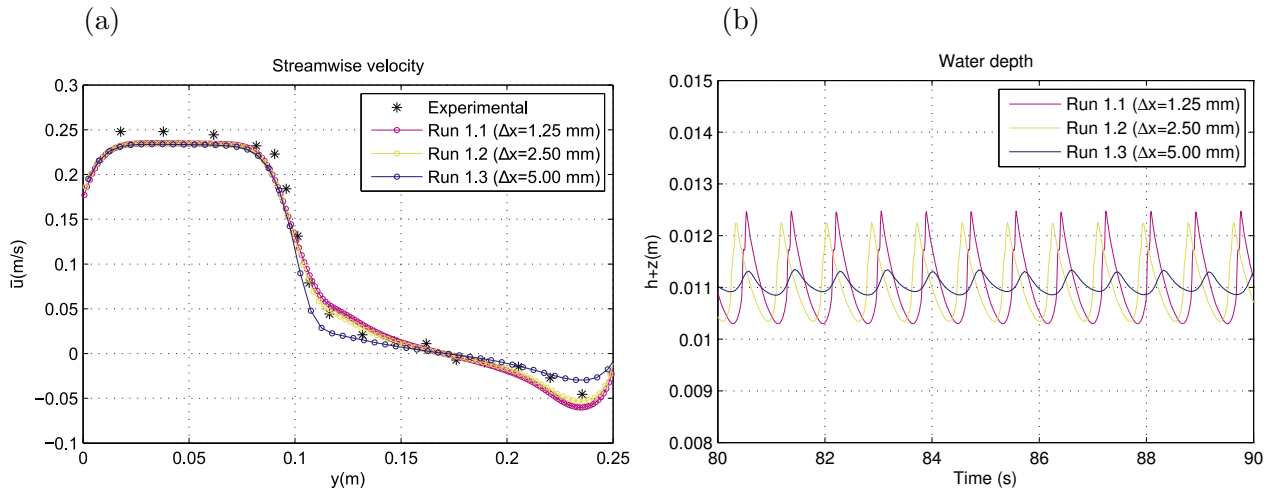
Figure 3: (a) Computed and measured time-averaged streamwise velocity along $T - T'$ for $\Delta x = 1.25$ (run 1.1), $\Delta x = 2.5$ (run 1.2) and $\Delta x = 5$ mm (run 1.3). (b) Mean water depth at the upstream edge of the cavity computed using $\Delta x = 1.25$ (run 1.1), $\Delta x = 2.5$ (run 1.2) and $\Delta x = 5$ mm (run 1.3). Time-averaged quantities are denoted by the overbar symbol $(\bar{\cdot})$.

The role of the order of accuracy of the numerical scheme was also investigated. A comparison of the results provided by the 3-rd order WENO-ADER scheme (run 1.2) and a 1-st order scheme (run 1.4), using a $\Delta x = 2.5$ mm grid, is presented in Figure 4. The numerical results evidence that a first order of accuracy is too diffusive to reproduce the standing gravity wave, since the shear instability at the opening of the cavity cannot be captured. Additionally, it is observed that the velocities inside the cavity, along the section $T - T'$, are underestimated by the 1-st order scheme. This scheme is thus not adequate to reproduce resonant flows. Only when using the RANS approach (i.e. when using adequate values for the turbulent viscosity), the 1-st order scheme is valid.

In [8], the authors provided measurements of the time evolution of the streamwise velocity magnitude at different locations along the shear layer. In particular, they define the points a, b and c, whose coordinates are provided in [8]. Such data allow to assess the validity of the numerical model to reproduce the vortex generation/amplification process and its coupling with the seiche.

Finally, and departing from the previous results, the best calibration of the URANS model was obtained and corresponds to run 1.5. The bottom and wall friction (n_b and n_w) and the turbulence parameters of the model (λ and β) were fine tuned to provide accurate results of the time-averaged velocities along the section $T - T'$ (Figure 5), assuming a realistic description of the time evolution of the velocity at the shear layer, when compared to the measurement in [8] (Figure 6). This case
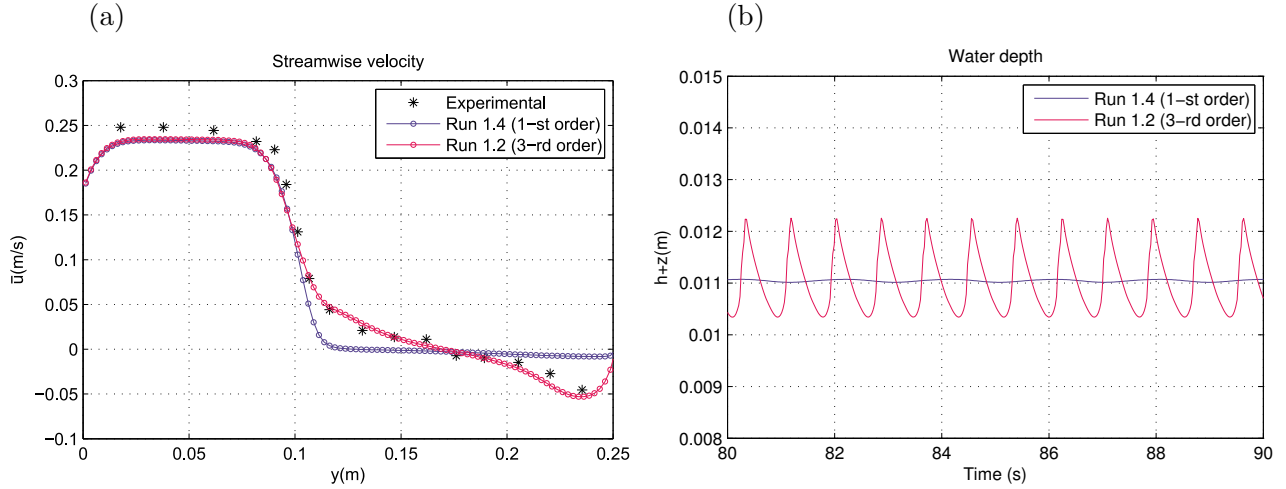
17

Figure 4: (a) Computed and measured time-averaged streamwise velocity along $T - T'$ for a 1-st order scheme (run 1.4) and 3-rd order scheme (run 1.2). (b) Mean water depth at the upstream edge of the cavity computed using a 1-st order scheme (run 1.4) and 3-rd order scheme (run 1.2). Time-averaged quantities are denoted by the overbar symbol ($\bar{\cdot}$).

corresponds to a URANS simulation where the horizontal eddies are practically resolved while small-scale dissipative effects are modelled by choosing a suitable parametrization of the turbulent viscosity.

The numerical results provided by the URANS simulation (run 1.5) are compared to the results provided by a pure RANS computation (run 1.6) in Figures 5 and 6. Note that the RANS approach provides a steady solution with no variation in time of the water level. The whole effect of the time fluctuating value of the water level is modelled and accounted for by the turbulence model. A comparison of the time-averaged longitudinal velocity along $T - T'$ is depicted in Figure 5 (a), showing that the URANS approach (run 1.5) provides accurate results in the main channel and in the shear layer, though it overstimates the velocity in the recirculation zone. On the other hand, the RANS approach (run 1.6) appears to be diffusive (due to excessive numerical viscosity) and inaccurate in the main channel and shear layer though it provides acceptable results inside the cavity. A comparison of the time-averaged velocity field for the URANS and RANS approaches (run 1.5 and 1.6 respectively) with the solution in [8] is presented in Figure 5 (b, c and d). It is observed that the velocity field provided by the proposed scheme when using the URANS model contains the same features than the solution in [8]. Inside the cavity, both solutions show the presence of a main vortex, referred to as S1, and three secondary eddies, denoted by S2, S3 and S4. The RANS model only shows the main vortex, S1, but the secondary eddies cannot be captured.

The lack of accuracy of the RANS model in the resolution of the shear layer is evidenced in Figure 6: the velocity at points a ($x = 0.175$ m, $y = 0.09$ m), b ($x = 0.200$ m, $y = 0.09$ m) and c ($x = 0.250$ m, $y = 0.09$ m), which is steady given the nature of RANS simulations, is lower than the time varying experimental data.

4.1.3. Case 2

In this section, numerical results for the case 2 (cavity length $L = 22.5$ m) in Table 1 are presented. The calibration chosen for Case 1 - run 1.5 is preserved to evidence the applicability of the numerical model to a different case. Details of the parameters for the simulation are summarized in Table 2. In run 2, a RANS simulation of the problem is carried out. To this end, a different configuration of the turbulence model is required in order to model all fluctuations in time. When considering the URANS approach (run 1), relatively small values of λ and β are used, so that the main coherent vortices are not damped and can be resolved by the model. For the RANS approach, such calibration constants must
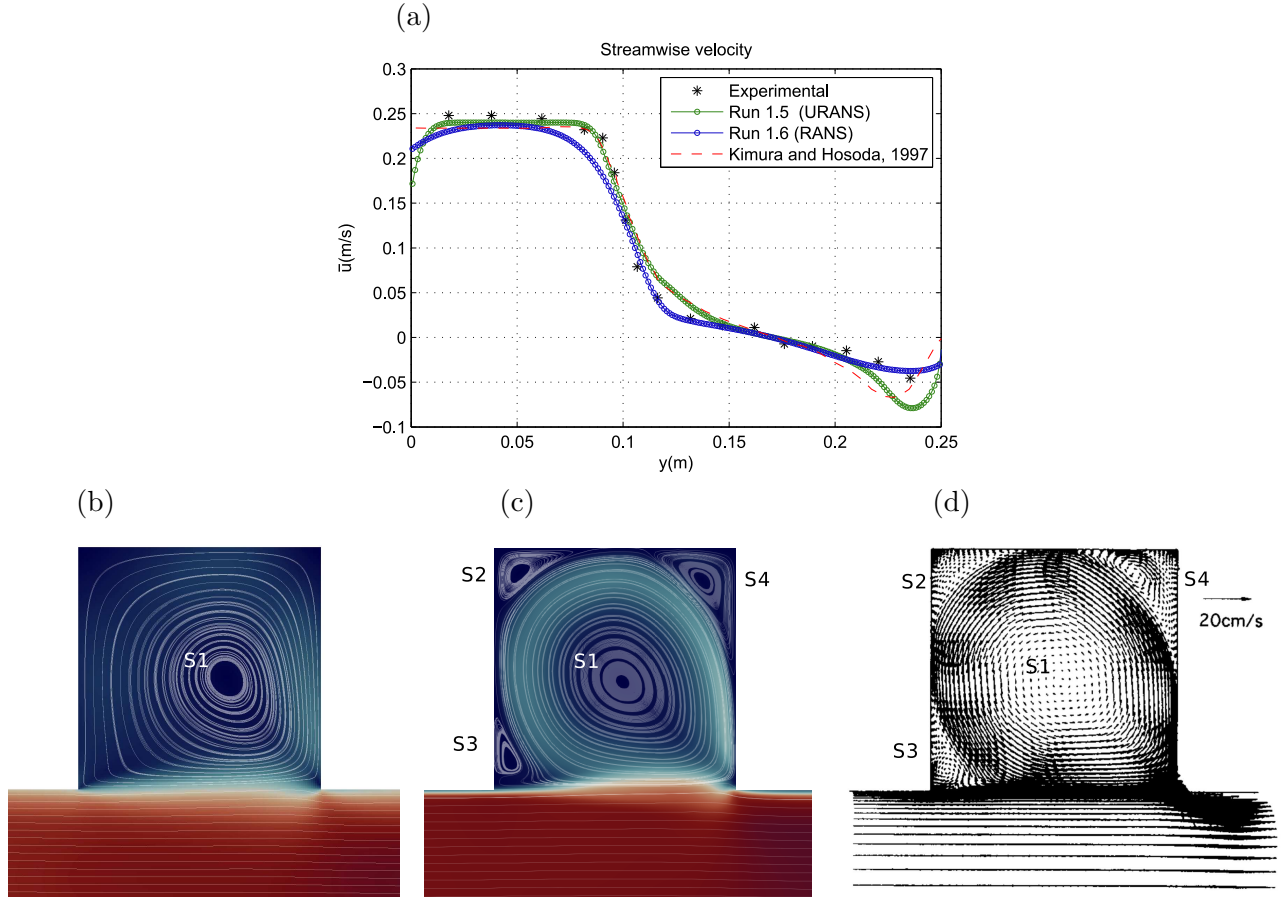
Figure 5: Computed and measured time-averaged streamwise velocity along $T - T'$ (a). Magnitude and streamlines of the time-averaged velocity provided by the RANS approach (b) and URANS approach (c). Numerical solution provided in [8] (d). The main vortical structure is denoted by S1 and the secondary eddies by S2, S3 and S4. Note that the bottom-right plot has been obtained from [8]. Time-averaged quantities are denoted by the overbar symbol ($\bar{\cdot}$).

be increased in order to damp any fluctuation and to model their effect as a pure diffusive process.

Run	Model	q_{bc} (l/s)	h_{bc} (cm)	ν (m^2/s)	λ	β	n_b	n_w	Δx (mm)	Order
2.1	URANS	0.747	2.02	1E-6	0.15	0.05	0.010	0.025	2.5	3
2.2	RANS	0.747	2.02	1E-6	1.5	2.0	0.010	0.025	2.5	1

Table 3: Numerical parameters for the turbulent model and the simulations.

In Figure 7 (a), the numerical solution for the time-averaged streamwise velocity component along $T-T'$ is compared with the measured and numerical solution provided in [8]. A top-view representation of the time-averaged velocity field for the RANS and URANS simulations, compared with the results provided in [8], is presented in Figure 7 (b, c and d). It is observed that the numerical solution provided by the proposed model matches the reference solution. The results provided by the RANS approach (run 2) evidence that the velocity gradient across the shear layer is smeared and the prediction of the flow field in the main channel is less accurate.

Figure 8 shows the evolution in time of the numerical and measured mean water surface elevation, h, and u velocity at point d. As mentioned before, only when using the URANS approach (run 2.1),
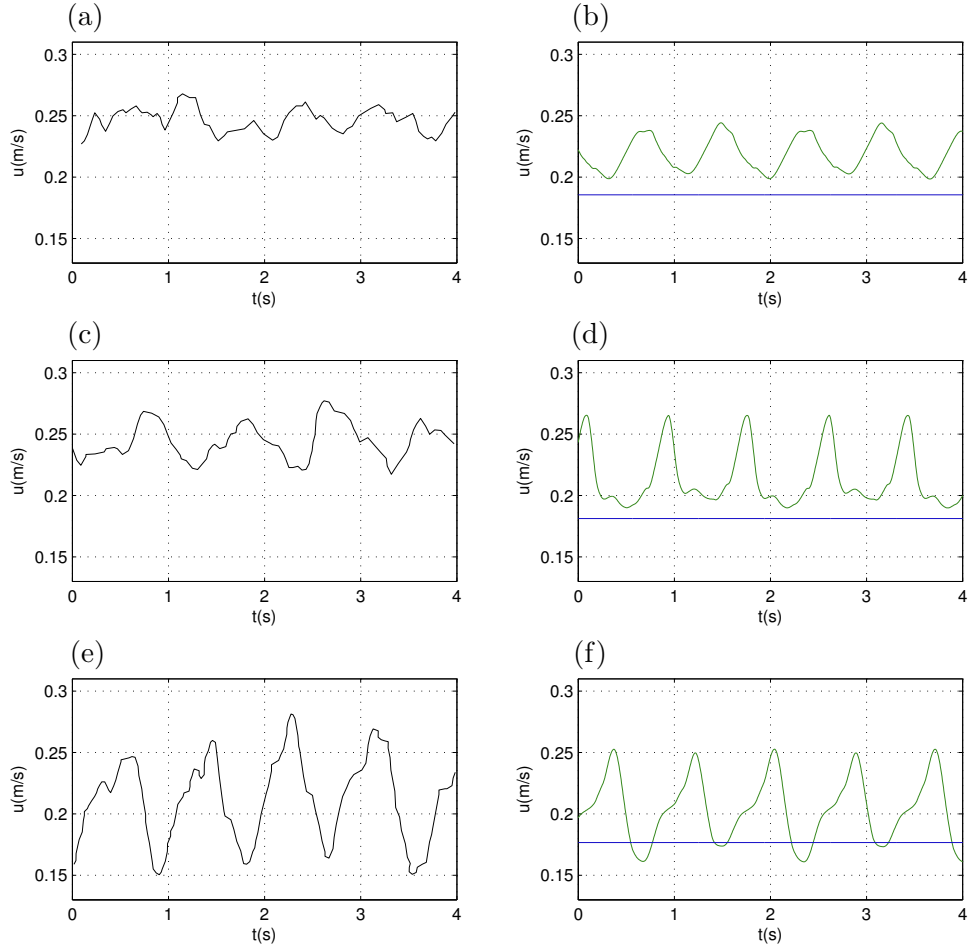
Figure 6: Measured (plots a, c and e) and numerical (plots b, d and f) evolution of the streamwise velocity in the x-direction at points a (plots a and b), b (plots d and d) and c (plots e and f). Results provided by URANS (run 1.5, green line) and RANS approaches (run 1.6, blue line).

temporal variations of the mean flow field are captured. As in [8], the oscillation of the predicted streamwise mean velocity, u, has a greater amplitude than in the experimental observations. This may be due to an excessive level of periodicity and coherence in the numerical solution, without extra oscillating modes, produced by an absence of vortex breakup mechanisms that would damp the periodic component associated to the seiche [50]. Figure 8 also shows that the RANS approach yields an steady solution which provides a better prediction of water depth and velocity, in terms of time-averaged values, than in Case 1.

The numerical results prove that the proposed WENO-ADER scheme reproduces the observed seiche, providing an accurate estimation of the frequency and amplitude of the oscillation, as well as the instantaneous and time-averaged magnitude of the velocities within an acceptable level of accuracy. Taking into account the results for Case 1 and 2 discussed above, we can conclude that the proposed numerical scheme is sufficiently valid to reproduce complex flow patterns in enclosed water bodies, involving the coupling of shear instabilities and gravity waves.

(a)

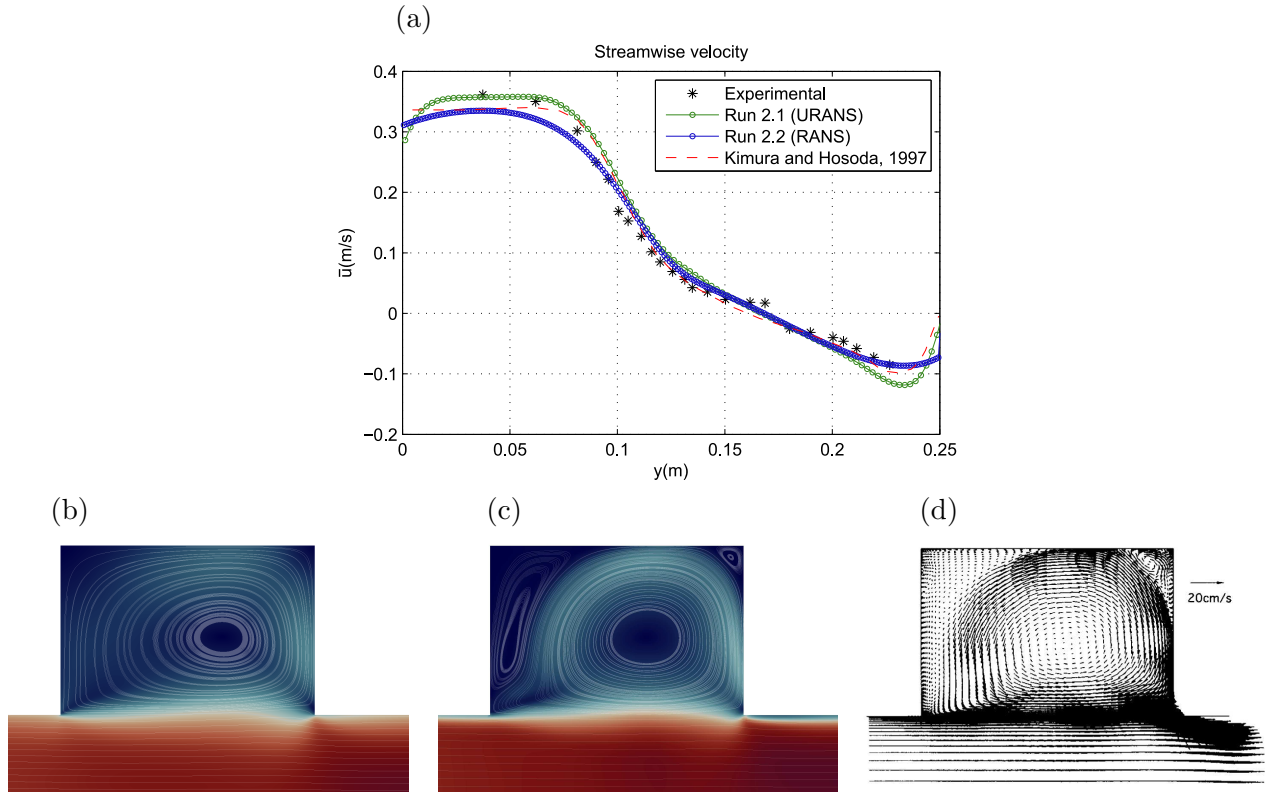Streamwise velocity

(b)　　　　　　(c)　　　　　　(d)

Figure 7: Computed and measured time-averaged streamwise velocity along $T - T'$ (a). Magnitude and streamlines of the time-averaged velocity field obtained by URANS (b) and RANS (c), compared to the time-averaged numerical velocity field provided in [8] (d). Time-averaged quantities are denoted by the overbar symbol ($\bar{\cdot}$).

4.2. Multiple lateral cavities

4.2.1. Problem definition

In this section, the proposed WENO-ADER scheme is applied to the resolution of the flow in channels with multiple lateral cavities. Such cavities are built in the banks of rivers to create harbors or to promote areas with hydraulic and morphological diversity that enhance habitat suitability. For instance, this is a very common measure to recover and revitalize riverine habitats that have degenerated because of anthropogenic activities (e.g. river channelization for different purposes such as land expansion, flood protection or agriculture) [11, 51].

The hydrodynamic response of lateral cavities is characterized by a main recirculation region that may trap the fine sediments travelling within the flow in the main channel as defined in [9, 41, 52]. In particular conditions, a seiche appears inside the cavities, which homogenizes the small-scale fluctuations in the flow and promotes vertical mixing, compromising the trapping efficiency of the cavities. Unlike in geometric configurations involving a single cavity, as those in the previous section, the interaction of multiple cavities has an additional effect in the propagation and formation of resonant waves.

The complex flow structures produced by the geometric configurations herein described challenge the prediction capabilities of the numerical methods and are thus considered in this section to evaluate the performance of the proposed numerical methods. Systematic laboratory tests in an open channel equipped with bank lateral embayments were carried out by Juez et al. [9, 41] for different geometric configurations. The hydrodynamic response of the configurations tested was assessed by means of
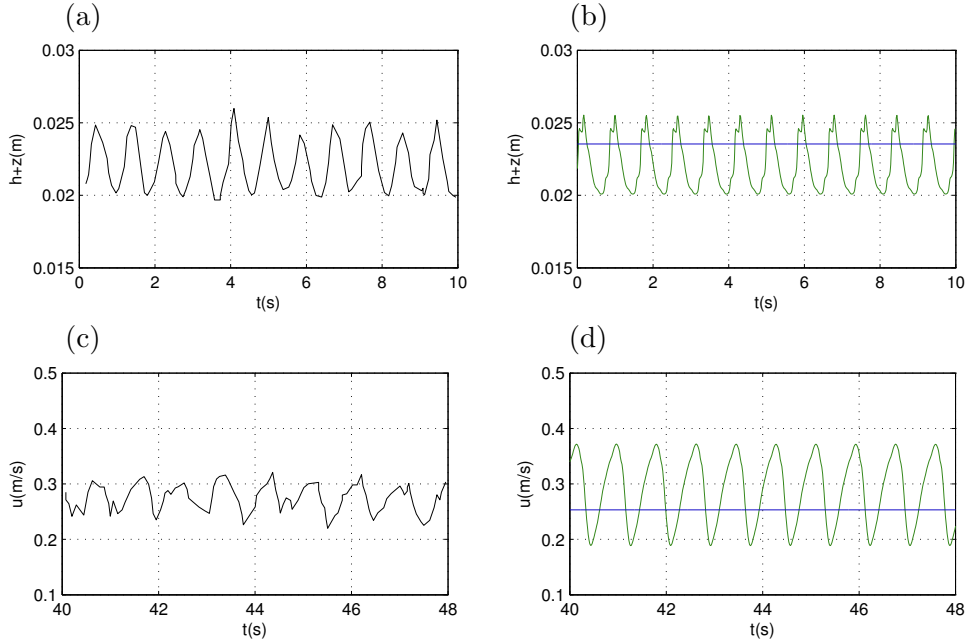
Figure 8: Experimental (a,c) and numerical (b,d) mean water surface elevation (a,b) and time evolution of mean streamise velocity (c,d) at point d. URANS approach in green line and RANS approach in blue line.

velocity (surface PIV) and water surface elevation (ultrasounds probes) measurements. The experimental results obtained in these tests are considered here as a benchmark. In particular, the flow for the geometric configurations 2.1 and 3.1 [9, 41] will be reproduced.

Comparison with experimental data will allow to explore the role of the turbulence model in the prediction of the frequency and amplitude of the seiche. The effect of the numerical diffusion in the solution, which is related to the grid size, is investigated.

A schematic representation of a sector of a channel with lateral cavities is depicted in Figure 9. The relevant dimensions, also represented in Figure 9, are the total width of the channel (base channel and cavities), B, the width of the base channel, b, the lateral width of the cavities, $W = (B - b)/2$, the length of the cavities, l, and the distance between cavities, L. The geometric configurations 2.1 and 3.1 [9, 41] depicted in Figure 10.

4.2.2. Geometric configuration 3.1

The geometric configuration 3.1 is characterized by a total channel width of $B = 1$ m, a base channel width of $b = 0.5$ m and a length of the cavities equal to their separation, that is $l = L = 0.5$ m. The geometry of the channel and the location of three numerical probes, P1, P2 and P3, measuring the water depth, are depicted in Figure 10 (b). The cavity where surface PIV measurements were carried out is highlighted in blue and experimental measurement of water depth was only done at the location of P1 and P3. The slope of the channel is 0.1% and the flow was configured to be uniform, with $h = 0.05$ m and $Q = 8.5$ l/s.

In this particular configuration, a seiche with a period of $T = 2.84$ s was observed [41]. The analytical estimation of the period of the seiche can be calculated with $T = 2B/nc$, setting $B = 1$ m and $h = 0.05$ m, and yields is $T = 2.86$ s. This result is in good agreement with the experimental measurement.

All simulations will be computed using the 3-rd order WENO-ADER scheme if no other method is specified. The simulation time is $t = 300$ s, which is sufficient for the seiche to be stable and allows

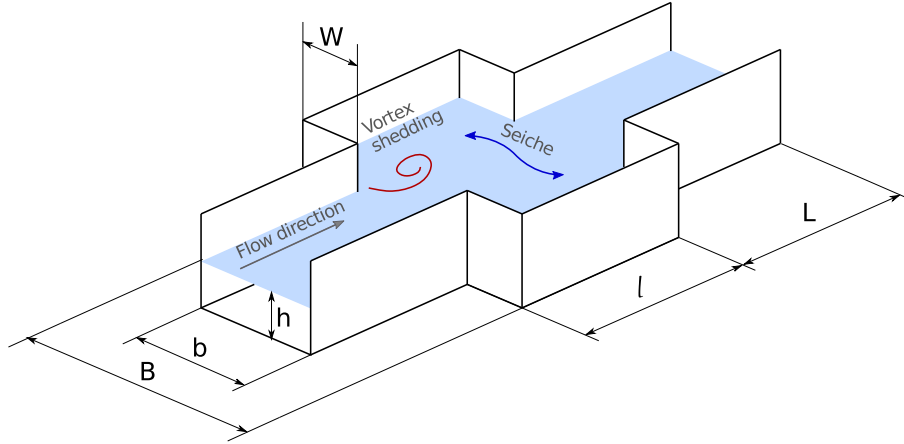Figure 9: Representation of a sector of the channel with lateral cavities including the relevant geometric dimensions and flow features.
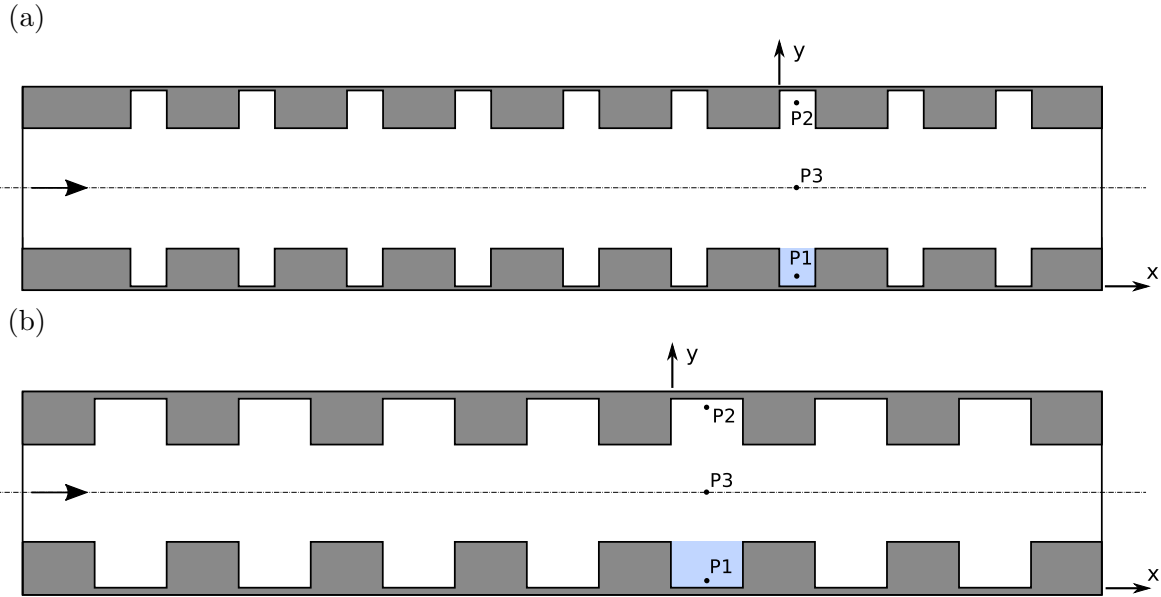
(a)

(b)

Figure 10: Representation of the channel configuration 2.1 (a) and 3.1 (b), including the location of the probes P1, P2 and P3. The cavity used in the experimental measurements is highlighted in blue.

to use an adequate time window for the time integration of the velocities. The computational domain is given by $\Omega = [0, 7.5] \times [0, 1]$ and four different cell sizes will be used, $\Delta x = 0.0125$ m, $\Delta x = 0.01$ m, $\Delta x = 0.00625$ m and $\Delta x = 0.005$ m. The stability condition is set to $CFL + Pe = 0.45$ for all simulations. The boundary conditions are given by a constant discharge of $hu = Q/b = 0.017$ m^2/s upstream and a constant water depth $h = 0.05$ m downstream. Note that the boundary conditions are imposed by means of the characteristic variables at the inlet and outlet cell interfaces.

The Manning coefficient on the channel bed is set to $n = 0.01$ sm$^{-1/3}$ and on the channel walls to $n = 0.03$ sm$^{-1/3}$ in the case of concrete (inner walls) or $n = 0.01$ sm$^{-1/3}$ in the case of glass (side walls). See [9, 41] for a detailed description of the experimental setup. The depth-averaged mixing length turbulence model is used, if no other method is specified, considering the following calibration $\lambda = 0.15$ and $\beta = 0.05$.

Remark that a initial perturbation in the transverse direction must be added in order to trigger the

presence of the seiche. Otherwise, the numerical solution is perfectly symmetrical and only longitudinal traveling waves are observed since the grid is also symmetric with respect to the channel longitudinal axis. Figure 11 shows the evolution in time of the difference $h_{P1} - h_{P2}$ for a simulation without initial perturbation and with a initial perturbation of $v = 0.008$ m/s. Note that the visualization of the difference $h_{P1} - h_{P2}$ allows to quantify the level of symmetry of the solution. Only when such difference is below machine precision, the solution is symmetric. Figure 11 (a) shows the solution for the whole simulation time. Figure 11 (b) shows a zoom of a small region of the unperturbed solution. The grid size is $\Delta x = 0.00625$ m. It is observed that only when the initial condition is perturbed, the span-wise symmetry is broken up and a coherent oscillation is observed. This oscillation represents the seiche. On the other hand, the unperturbed solution also shows an oscillation, as shown in the zoomed plot. This oscillation has an amplitude of the magnitude of machine truncation errors. It can be thus considered numerical noise.

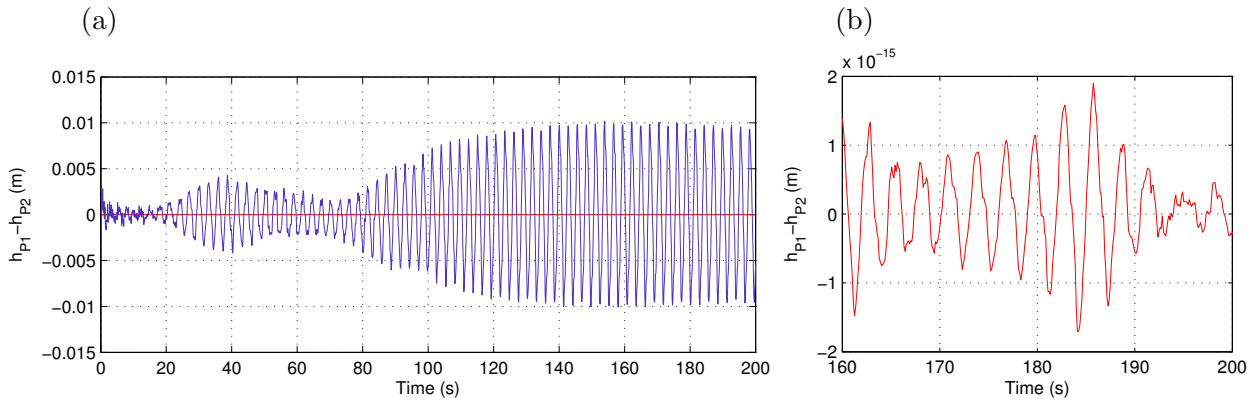(a)   (b)

Figure 11: (a) Evolution in time of the mean water depth difference between points P1 and P2, $h_{P1} - h_{P2}$. The red line is the numerical solution when no initial perturbation is added whereas the blue line represents the numerical solution when adding a initial perturbation of $v = 0.008$ m/s. (b) Zoomed region of the unperturbed solution that shows that $h_{P1} - h_{P2}$ is below machine precision.

The role of the turbulence model in the numerical prediction of the seiche is now investigated. In Figure 12, the evolution in time of the numerical mean water depth at P1, P2 and P3 is depicted for the three different meshes described above. In the upper row, results obtained when using the depth-averaged mixing length turbulence model ($\lambda = 0.15$ and $\beta = 0.05$) are presented, while in the bottom row, results without turbulence model are depicted. It is observed that the use of the turbulence model in combination with a high order of accuracy in the numerical integration is crucial for a suitable prediction of the water depth oscillation. Only with the help of a turbulent model, the numerical solution can become mesh independent, as observed in Figure 12. On the other hand, if the turbulence model is not considered, the periodicity of the oscillation is destroyed as the mesh is refined due to a lack of dissipation (the numerical diffusion is highly reduced and there is no other source of diffusion). This is also evidenced in Figure 13, where the power spectrum of the signals, computed by means of an FFT algorithm, is depicted. It is observed that the analytical estimation of the period of the seiche is well captured when using the turbulence model, with independence of the grid.

A plot of the evolution of the peak-to-peak amplitude, $h_{pp} = 2\sqrt{2}\sigma_h$ (where σ_h is the standard deviation of h in time), with respect to the cell size is presented in Figure 14. The results are computed using the depth averaged mixing length turbulence model ($\lambda = 0.15$ and $\beta = 0.05$) and evidence that a resolution of $\Delta x = 0.00625$ m is sufficient to avoid any dependence with the grid. This can be observed as the convergence of h_{pp} at P1 to a virtually constant value. Note that the factor $2\sqrt{2}$ is the ratio between the peak-to-peak amplitude and the standard deviation of a sinusoidal signal. In this case, the

24

⁶²¹ seiche is close to a sinusoidal fluctuation, hence h_{pp} will be an adequate estimation of the peak-to-peak
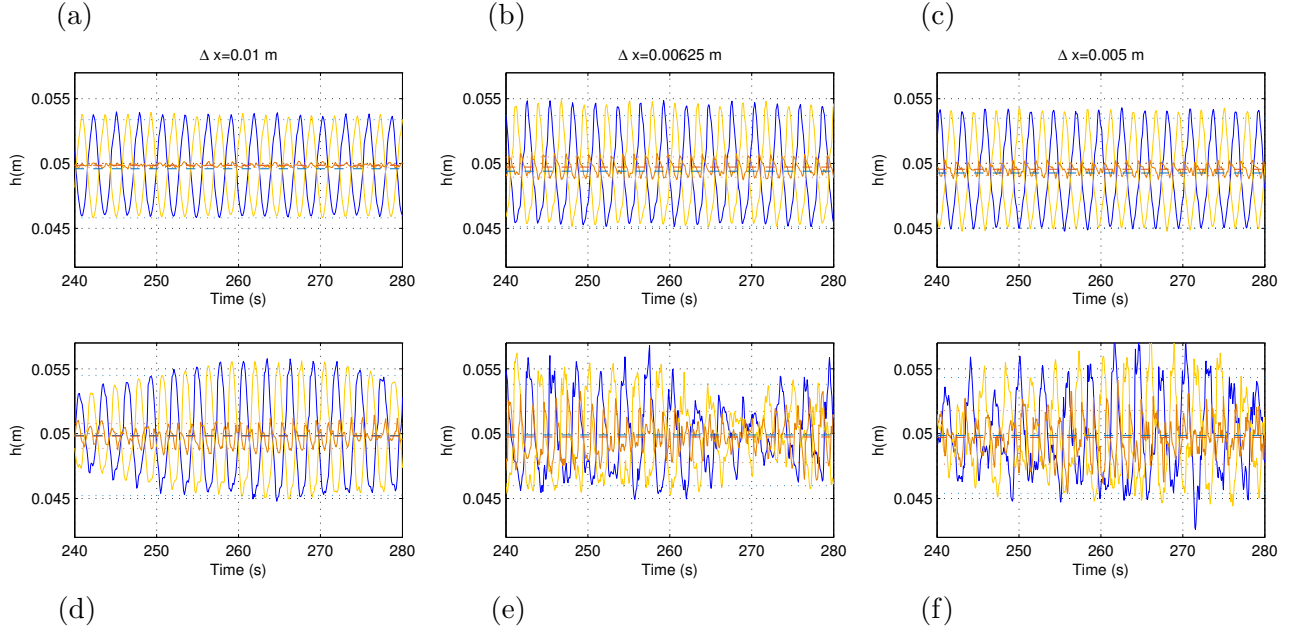⁶²² amplitude.

Figure 12: Mean water depth evolution in time at P1 (blue), P2 (yellow) and P3 (orange), computed by the 3-rd order WENO-ADER scheme in three different meshes with $\Delta x = 0.01$ m (a,d), $\Delta x = 0.00625$ m (b,e) and $\Delta x = 0.005$ m (c,f), using the depth-averaged mixing length turbulence model ($\lambda = 0.15$ and $\beta = 0.05$) (a,b,c) and without using any turbulence model ($\lambda = \beta = 0$) (d,e,f).
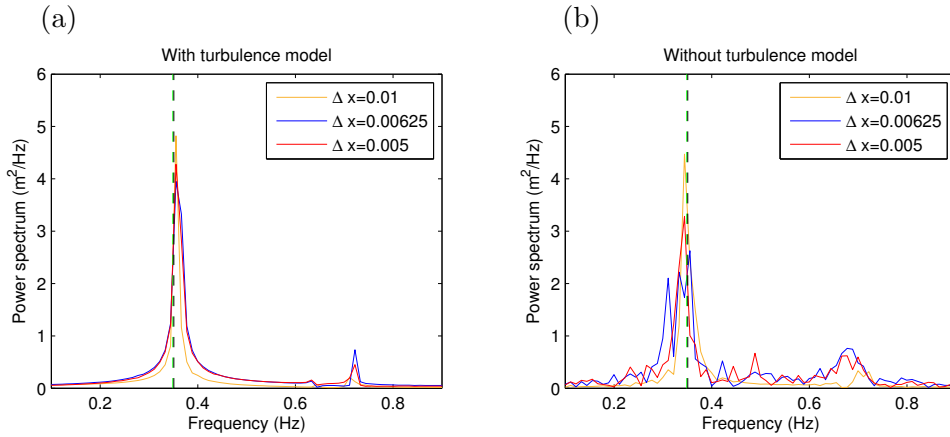
Figure 13: Power spectrum density distribution of the mean water depth fluctuation, measured at P1, for the case with turbulence model (a) and without turbulence model (b). The analytical and experimental frequency of the seiche are depicted with a black and green dashed line, respectively.

⁶²³ A comparison between the experimental water depth oscillation, measured at P1 and P3, and the
⁶²⁴ numerical prediction is depicted in Figure 15. It is again observed that the numerical model correctly
⁶²⁵ reproduces the frequency and amplitude of the seiche at both locations.

⁶²⁶ The time-averaged velocity field inside the cavity highlighted in Figure 10 was experimentally
⁶²⁷ assessed using a surface PIV technique. A comparison between the experimental measurements and the
⁶²⁸ numerical estimation of the velocity inside the cavity is presented in Figure 16. The numerical results
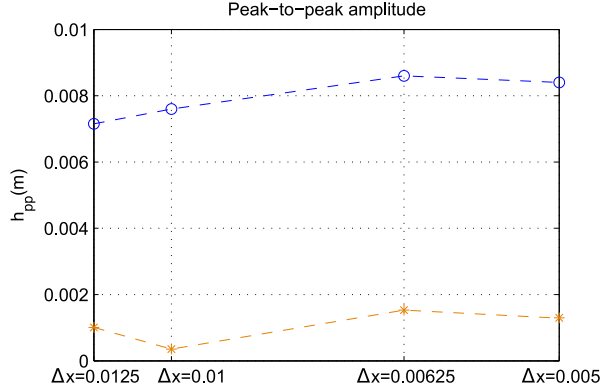
25

Figure 14: Plot of the peak-to-peak water depth amplitude, $h_{pp} = 2\sqrt{2}\sigma_h$, at P1 (blue) and P3 (orange), against the cell size. The solution is computed using the 3-rd order WENO-ADER scheme and the depth-averaged mixing length turbulence model.
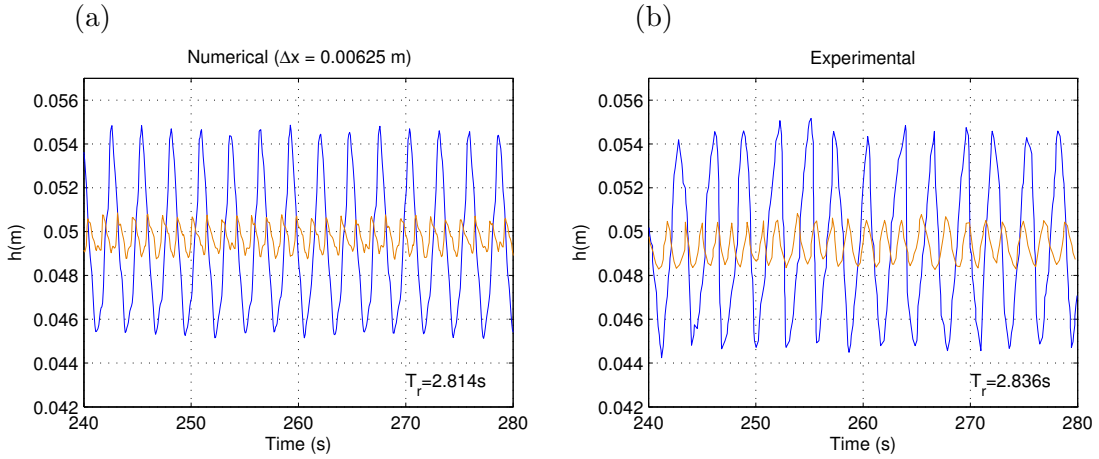

Figure 15: Numerical (a) and experimental (b) mean water depth evolution in time at P1 (blue) and P3 (orange). The numerical solution is computed using the 3-rd order WENO-ADER scheme and the depth-averaged mixing length turbulence model, using $\Delta x = 0.00625$ m. The period of the seiche is obtained using an FFT algorithm.

are computed using $\Delta x = 0.0625$ m. Figure 16 (a and b) shows a 2D comparison of the y component of the time-averaged velocity field. It evidences that the numerical model is able to reproduce the recirculating flow inside the cavity. A more quantitative comparison is presented in Figure 16 (c and d), where cross sectional representations of the measured and computed time averaged velocities are plotted. The time averaged streamwise velocity is plotted over the y direction at $x = 0.125, 0.25, 0.375$ m, whereas the time averaged spanwise velocity is plotted over the x direction at $y = 0.05, 0.125, 0.2$ m. It is observed that the numerical model slightly overpredicts the magnitude of the velocity in the recirculation region, if compared to the surface PIV measurements.

4.2.3. Geometric configuration 2.1

The geometric configuration 2.1 is characterized by a total width of the channel $B = 1$ m, a width of the base channel $b = 0.6$ m, a length of the cavities equal to $l = 0.25$ m and a separation between cavities of $L = 0.5$ m. The slope of the channel is 0.1% and the flow was configured with $Q = 8.5$ l/s and $h = 0.048$ m at the outlet. In this particular configuration, a periodic seiche was not reported [41]. The numerical solution was computed again using the 3-rd order WENO-ADER scheme. The simulation time is $t = 300$ s and the computational domain is given by $\Omega = [0, 7.5] \times [0, 1]$. The
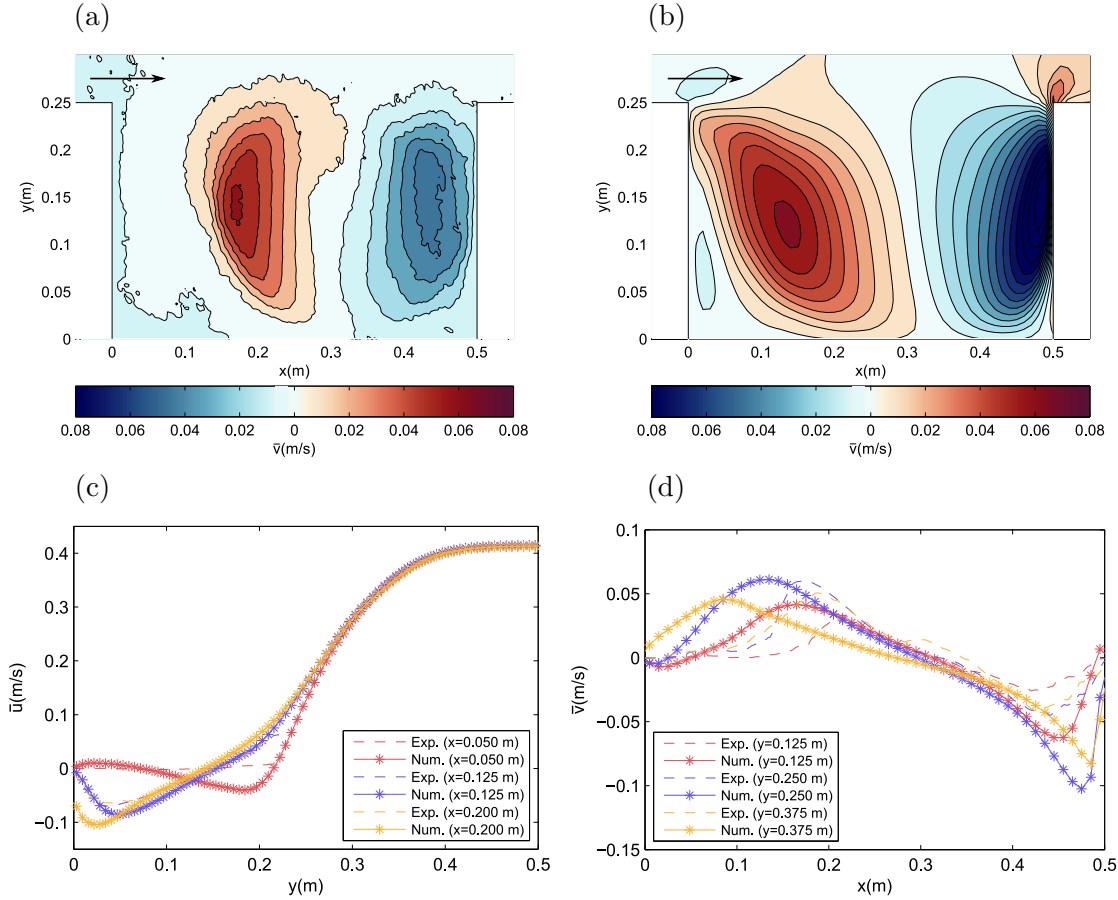
Figure 16: Measured (a) and computed (b) time-averaged spanwise velocity inside a cavity. Cross sectional representation of the measured and computed streamwise time-averaged velocity, along the y direction (c) and spanwise time-averaged velocity, along the x direction (d). Time-averaged quantities are denoted by the overbar symbol ($\bar{\cdot}$).

boundary conditions are given by a constant unit discharge of $hu = Q/b = 0.0141\bar{6}$ m^2/s upstream and a constant water depth $h = 0.048$ m downstream.

The Manning coefficient on the channel bed is set to $n = 0.01$ sm$^{-1/3}$ and on the channel walls to $n = 0.03$ sm$^{-1/3}$ in the case of concrete (inner walls) or $n = 0.01$ sm$^{-1/3}$ in the case of glass (side walls). The depth-averaged mixing length turbulence model is used with the following calibration $\lambda = 0.15$ and $\beta = 0.05$.

As in the previous case, the time-averaged velocity field inside one of the cavities is experimentally assessed using surface PIV. A comparison between the experimental measurements and the numerical estimation of the velocity inside the cavity is presented in Figure 17. The numerical results are computed using $\Delta x = 0.005$ m. Figure 17 (a and b) shows a 2D comparison of the y component of the time-averaged velocity. In Figure 17 (c and d), a cross sectional representation of the measured and computed time-averaged velocities are plotted. The streamwise component of the velocity is plotted over the y direction at $x = 0.0625, 0.125, 0.1875$ m. In addition, the spanwise component of the velocity is plotted over the x direction at $y = 0.05, 0.1, 0.15$ m. As in the geometric configuration 3.1, it is observed that the numerical results yield to a higher velocity magnitude in the recirculation region, specially near the downstream wall.

The calibration found in this work for the horizontal eddy viscosity coefficient in URANS simulation (i.e. $\beta = 0.05$) is consistent with previous literature as the coefficient βl_s^2 is of the order of magnitude
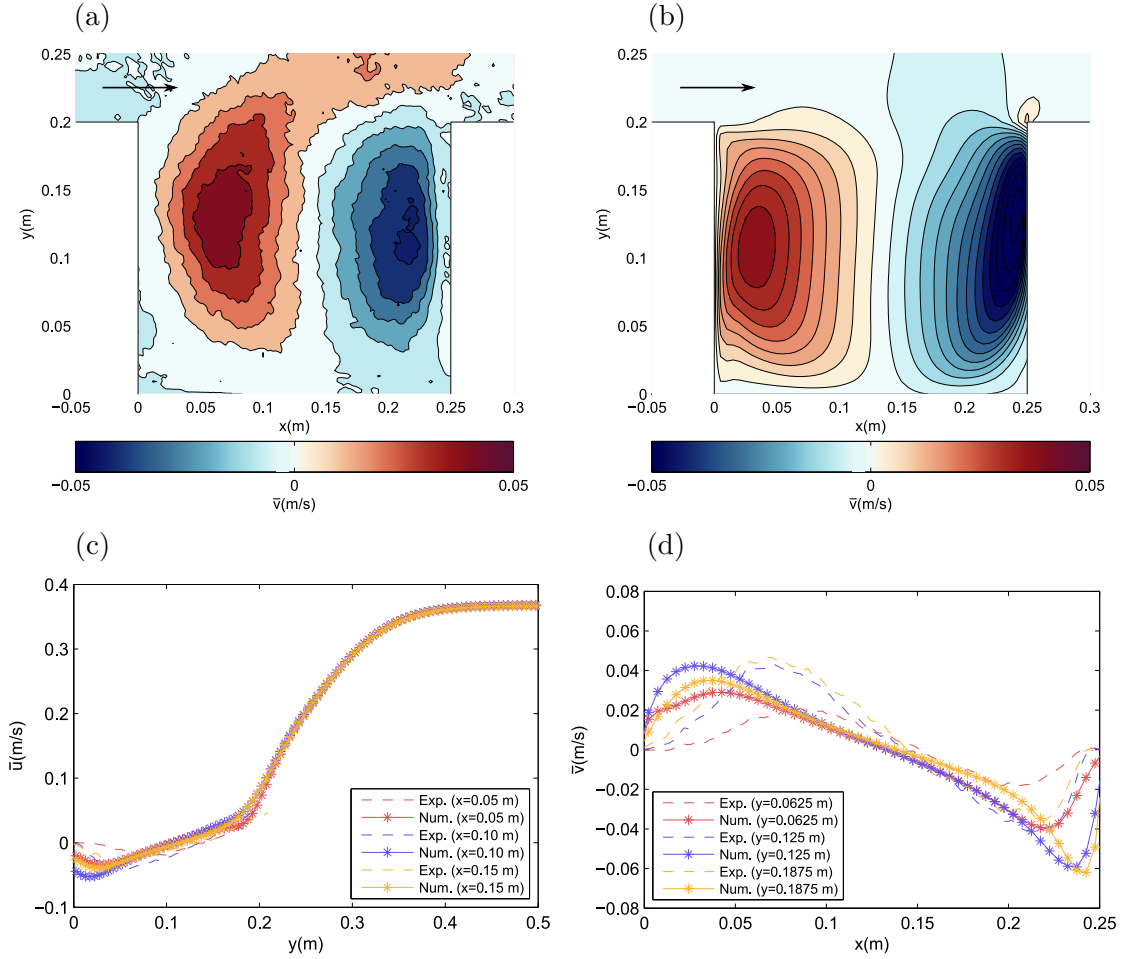
Figure 17: Measured (a) and computed (b) time-averaged spanwise velocity inside a cavity. Cross sectional representation of the measured and computed time-averaged streamwise velocity, along the y direction (c) and time-averaged spanwise velocity, along the x direction (d). Time-averaged quantities are denoted by the overbar symbol ($\bar{\cdot}$).

of $C_s \Delta x$. For instance, $\beta l_s^2 \sim 10^{-6}$ for cases 2.1 and 3.1, which is in good agreement with $C_s \Delta x$ for the selected grids (i.e. $\Delta x = 0.005$ m and $\Delta x = 0.00625$ m for cases 2.1 and 3.1, respectively) and for C_s inside the expected range, according to [45].

5. Concluding remarks

A depth averaged 2D URANS hydrodynamic solver based on an arbitrary order augmented WENO-ADER scheme for the SWE is designed for the resolution of turbulent shallow flows. A large extent of the large-scale 2D turbulence spectrum is thus resolved thanks to the high accuracy of the numerical scheme. Conversely, depth averaged calculations do not resolve 3D turbulence and the modelling of the unresolved subdepth-scale of 3D turbulence is required. Part of the dissipation produced by this effect is accounted for by means of friction losses, using a friction source term in the momentum equations. However, this was not sufficient hence an eddy viscosity model, related to the friction velocity and water depth, is used. The proposed model is also able to compute RANS simulations by means of including an extra contribution in the eddy viscosity due to local variations of the horizontal velocity.

The depth-averaged mixing length model is used for the evaluation of the eddy viscosity both for the RANS and URANS approaches. When using the RANS approach, both 3D and 2D turbulence is

modelled. When using the URANS methdology, 3D turbulence is modelled as in the RANS approach and 2D turbulence is mostly resolved. Only the smallest horizontal scales (sub-grid scales) cannot be resolved and have to be modelled using a horizontal eddy viscosity coefficient. In URANS simulation, such approach can be regarded as a sub-grid model for the unresolved horizontal 2D scales.

Concerning the numerical scheme, a WENO-ADER method is used. It can be regarded as an arbitrary order extension of the first order Godunov's method. The WENO reconstruction is used to provide an arbitrary order of accuracy in space, avoiding Gibbs oscillations. The ADER approach allows to extend the updating scheme to arbitrary order in time without needing extra sub-steps. Thanks to the use of WENO-ADER schemes, the numerical diffusion and dispersion are reduced to the desired level so that the scheme is able to resolve small-scale features of the flow. This makes such schemes suitable for the resolution of 2D turbulence, as it is possible to control to which extent the energy spectrum is resolved or modelled. As a result, the numerical scheme shows convergence with mesh refinement even in cases with transient propagation of gravity waves and shedding of vortices.

Different approaches for the numerical approximation of the turbulent diffusion terms are assessed. The use of a WENO-based reconstruction of the derivatives is not suitable due to the non-linear limiting of sharp gradients provided by the WENO method when the length scales of the velocity gradients are lower than the cell size, making the solution not consistent with physics. On the contrary, the linear version of such method circumvents this problem and provides a more accurate solution. For the sake of simplicity and efficiency, a second order discretization using centered differences is chosen.

Bed variations are also considered in the SWE in order to account for a complex bathymetry. The thrust exerted by the bed slope is accounted for as a source term in the momentum equations. The ARoe solver, in combination with a particular integration of the source terms of arbitrary order, is used to satisfy the well-balanced property and preserve the lake-at-rest equilibrium state. The DRP is solved by means of the ARL solver, which is a high order extension of the ARoe solver.

The performance of the proposed model is assessed by comparing with experimental data. Four benchmark cases, two of them involving a channel with a single lateral cavity, and other two involving a channel with multiple lateral cavities, are used. The numerical results evidence that the URANS model accurately reproduces both longitudinal and transversal seiche waves and provides an accurate description of the flow field. In certain cases, the magnitude of the time-averaged velocity in the recirculation zones is slightly overestimated. This is presumably due to the non-purely 2D nature of the flow, thus it has been more clearly noticed in cases where the ratio between the horizontal dimensions of the cavity and the flow depth is low. When considering the RANS approach, the scheme reproduces the measured time-averaged velocity field, but fluctuations in time and seiches cannot be reproduced.

It is observed that the amplitude and shape of the seiche is, in general, sensitive to the parameters of the turbulence model. However, the frequency keeps a quasi-constant value regardless the changes in the calibration of the turbulence model. The numerical frequency is systematically in good agreement with the theoretical/experimental estimation. Furthermore, it is evidenced that there is no need to use very fine meshes thanks to the WENO reconstruction technique and the ADER time stepping. A number of 40 to 60 cells along the width of the cavity has been reported in all tests to be sufficient to reproduce the experimental data.

The proposed model offers a suitable solution for the computation of turbulent shallow flows with high order of accuracy, allowing to resolve a large extent of the 2D turbulence spectrum, while modelling the 3D small scale turbulence. The model is explicit and fully discrete, and preserves the fundamental equilibrium states of interest (e.g. lake-at-rest) thanks to a robust integration of the source terms that ensure high order of accuracy without loosing stability. The framework for the construction of arbitrary order schemes has been presented, allowing to find a good compromise between the accuracy and the computational cost of the scheme. The model is suitable for coarse computational meshes, thanks

725 to (a) the high order of accuracy and (b) to the accurate modelling of the sub-grid unresolved physics
726 (i.e. wall and bottom friction and small scale turbulence), using high order sub-cell reconstructed
727 data. This makes the proposed model a useful tool for realistic scenarios, comprising large spatial
728 and temporal scales, with an eventual application to more complex phenomena (e.g. geomorphological
729 applications). As a future work, the development of a more accurate wall friction model that relates
730 the wall roughness and the mixing length will be considered. The design of a wall friction law that
731 spans over the cells within the boundary layer will be investigated in the framework of the proposed
732 model.
733

Appendix A. Details on the numerical approximation of the diffusion terms

740 To show the numerical performance of the two different approaches for the reconstruction of the
741 spatial gradients outlined in the text, a numerical experiment involving a shear flow is presented. Let
742 us consider a pure shear flow with constant water depth depth in the streamwise direction, x, defined
743 in the semi-infinite domain $\Omega = [-\infty, \infty] \times [0, 1]$. The transverse velocity, v, is nil and the streamwise
744 velocity, u, is equal to -0.001 if $0 \leq y \leq 0.5$ and 0.001 if $0.5 < y \leq 1$. Bed slope and bed friction are
745 not considered. All variations in x are nil. This problem can be reduced to a 1D problem in the y
746 direction and Equation (1)–(2) becomes:

$$\frac{\partial(hu)}{\partial t} + \frac{\partial(huv)}{\partial y} = \nu h \frac{\partial^2 u}{\partial y^2} \tag{A.1}$$

747 For the conditions of the problem, the solution of (A.1) is given by:

$$hu(y, t) = 5 \cdot 10^{-4} erf\left(\frac{y - 0.5}{2\sqrt{\nu t}}\right) \tag{A.2}$$

748 and it leads to $v = 0$. In discrete form, Equation (A.1) becomes:

$$(hu)_j^{n+1} = (hu)_j^n + \frac{\Delta t}{\Delta x}\left((huv)_{j+1/2}^\star - (huv)_{j-1/2}^\star\right) + \frac{1}{\Delta x}\bar{D} \tag{A.3}$$

749 where

$$\bar{D} \approx \int_{t^n}^{t^{n+1}} \int_{y_{i-1/2}}^{y_{i+1/2}} \nu h \frac{\partial^2 u}{\partial y^2} dy dt \tag{A.4}$$

750 As in the analytical solution, when $v = 0$, the numerical flux for the shear momentum provided by
751 the ARoe solver, $(huv)_{j+1/2}^*$, is nil. This is straightforward to prove by analyzing the third component
752 of the y-version of (33), which involves the numerical flux for the shear momentum:

$$(huv)_{j+1/2}^\star = (huv)_{j+1} - \widetilde{v}\left(\frac{\widetilde{u}\delta h}{2} - \frac{\widetilde{v}\delta h - \delta(hv)}{2\widetilde{c}}\widetilde{u} + \delta(hu) - \widetilde{u}\delta h\right) - \widetilde{c}\left(\frac{\widetilde{u}\delta h}{2} - \frac{\widetilde{v}\delta h - \delta(hv)}{2\widetilde{c}}\widetilde{v}\right), \tag{A.5}$$

753 If inserting $\widetilde{v} = \delta h = \delta(hv) = 0$ in Equation (A.5), it yields to:

30

$$(huv)^{\star}_{j+1/2} = (huv)_{j+1} = 0 \tag{A.6}$$

hence, no shear momentum will be transferred across the interface in the numerical solution due to convective transport. Therefore, Equation (A.3) becomes:

$$(hu)^{n+1}_j = (hu)^n_j + \frac{1}{\Delta x}\bar{D} \tag{A.7}$$

The term $\bar{D}$ must be numerically approximated by using one of the options described before. If choosing the first option, based on the sub-cell derivative reconstruction procedure in [48], $\bar{D}$ yields to:

$$\bar{D} = \Delta t \nu h \left(\left(\partial_y u + \sum_{k=1}^{K} \partial_t^k(\partial_y u)\frac{\Delta t^k}{(k+1)!} \right)_{j_N} - \left(\partial_y u + \sum_{k=1}^{K} \partial_t^k(\partial_y u)\frac{\Delta t^k}{(k+1)!} \right)_{j_S} \right) \tag{A.8}$$

where the subscript N and S stand for north and south, with reference to the cell center. For instance, $(\partial_y u)_{j_N}$ is the sub-cell spatial derivative reconstruction at $y = y_{j_N}$. Note that this numerical sub-cell derivative can be reconstructed departing from data provided either by a WENO reconstruction or by an optimal polynomial reconstruction.

On the other hand, if choosing centered differences in Equations (45)–(50), $\bar{D}$ yields to:

$$\bar{D} = \Delta t \nu h \left(\frac{u_{j+1} - u_j}{\Delta x} - \frac{u_j - u_{j-1}}{\Delta x} \right) \tag{A.9}$$

Numerical results for the problem configuration detailed above, comparing the performance of the different approximations of the diffusion terms, are presented in Figure A.18. Four different tests, listed in Table A.4, are carried out. The first test does not consider any diffusion, hence the numerical scheme must preserve the discrete equilibrium, according to Equation (A.3). This is evidenced in Figure A.18 (a), which shows that the exact initial equilibrium is maintained and that there is no mixing across the shear layer.

On the other hand, tests 2, 3 and 4 do involve a nonzero viscosity. Test 2 is is based on the sub-cell WENO derivative reconstruction in (A.8) and, as expected, the solution in Figure A.18 (c) evidences that such method prevents the diffusive mixing across the discontinuity. The initial equilibrium is maintained since the reconstructed spatial gradients (and their higher order time derivatives) are nil in the whole domain, $(\partial_y u)_{j_{(\cdot)}} = 0$, with independence of the order of accuracy. Therefore, the method is unable to reproduce the analytical solution.

Test 3 is based on the same sub-cell derivative reconstruction approach, but using an optimal polynomial reconstruction rather than the WENO reconstruction. In this case, the derivatives at the discontinuities are properly approached, hence the method is more adequate to compute the diffusion terms. Numerical results for a 3-rd and 5-th order scheme are presented in Figure A.18 (d).

In Test 4, the diffusion terms are computed by means of centered differences in (A.9). As in Test 3, this method is able to accurately reproduce the analytical solution as depicted in Figure A.18 (b).

The numerical results evidence that the centered differences approach provides a lower accuracy than the the sub-cell derivative reconstruction method. However, the differences in accuracy of such approaches for the particular application of this methods will be negligible when compared to the numerical error of the convective terms. Furthermore, carrying out a sub-cell derivative reconstruction based on the optimal polynomial reconstruction supposes an added computational expense. Therefore, the centered differences approach is chosen for the particular applications herein considered.

Test	ν	Approximation of diffusion terms	Δx	Reconstruction order
1	0	None	0.02	-
2	0.001	Sub-cell derivative reconstruction (WENO limiting)	0.02	3-rd, 5-th
3	0.001	Sub-cell derivative reconstruction (optimal rec.)	0.05	3-rd, 5-th
4	0.001	Centered differences	0.05	2-nd

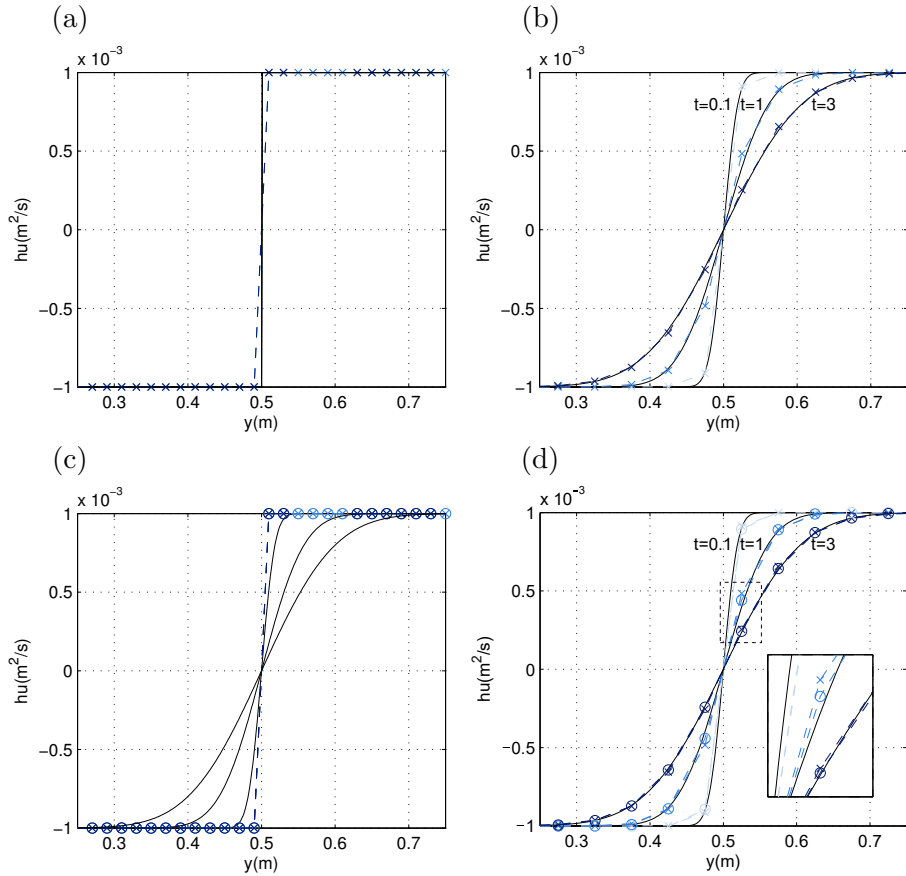Table A.4: Numerical tests to assess the validity of the approximation of the diffusion term.

Figure A.18: Cross sectional representation of the exact (solid line) and numerical hu in the y direction for test 1 (a), test 2: sub-cell derivative reconstruction with WENO limiting (c), test 3: sub-cell derivative reconstruction with optimal reconstruction (d) and test 4: centered differences (b). The numerical solution is presented at $t = 0.1, 1, 3$ s. Crosses and circles stand for 3-rd and 5-th order solutions, respectively.

References

References

[1] G. Jirka and W. Uijttewaal, Shallow Flows: a definition, in GH Jirka and WSJ Uijttewaal (eds), Shallow Flows. CRC Press / Balkema - Taylor and Francis Group, Leiden, International symposium on shallow flows, Delft, 2003.

[2] W. Uijttewaal, Hydrodynamics of shallow flows: application to rivers, Journal of Hydraulic Research, 52 (2014) 157-172.

[3] K. Nadaoka, H. Yagi, Shallow-water turbulence modeling and horizontal large-eddy computation of river flow, Journal of Hydraulic Engineering, 124 (1998) 493–500

[4] C. Juez, M. A. Hassan, M. J. Franca, The origin of fine sediment determines the observations of suspended sediment fluxes under unsteady flow conditions, Water Resources Research, 54 (2018) 5654–5669.

[5] E. Langendoen, C. Kranenburg, R. Booij, Flow patterns and exchange of matter in tidal harbours, Journal of Hydraulic Research, 32 (1994) 259–270.

[6] P. J. Wood and P. D. Armitage, Biological effects of fine sediment in the lotic environment, Environmental Management, 21 (1997) 203–217.

[7] V. Nikora, I. McEwan, S. McLean, S. Coleman, D. Pokrajac, R. Walters, Double-averaging concept for rough-bed open-channel and overland flows: Theoretical background. Journal of Hydraulic Engineering, 133 (2007) 873-883.

[8] I. Kimura, T. Hosoda, Fundamental properties of flows in open channels with dead zone, Journal of Hydraulic Engineering 123 (1997) 98–107.

[9] C. Juez, M. Thalmann, A. J. Schleiss, M. J. Franca, Morphological resilience to flow fluctuations of fine sediment deposits in bank lateral cavities, Advances in Water Resources, 115 (2018) 44-59.

[10] D. Bouffard and A. Wüest, Convection in lakes, Annual Review of Fluid Mechanics 51 (2019) 189-215.

[11] I. Nezu and K. Onitsuka, PIV Measurements of side-cavity open-channel flows. Wando model in rivers, Journal of Visualization, 5 (2002) 77–84.

[12] W. Rodi, G. Constantinescu, T. Stoesser, Large-eddy simulation in hydraulics, IAHR-monograph, CRCPress/Balkema, The Netherlands (2013).

[13] A. McCoy, G. Constantinescu and L.J. Weber, Numerical Investigation of Flow Hydrodynamics in a Channel with a Series of Groynes, Journal of Hydraulic Engineering, 134 (2008) 157-172.

[14] M. Sanjou, I. Nezu, Large eddy simulation of compound open-channel flows with emergent vegetation near the floodplain edge, 9th International Conference on Hydrodynamics. Shanghai, China, (2010) 565–569.

[15] R. J. McSherry, K. V. Chua, T. Stoesser, Large eddy simulation of free-surface flows, Journal of Hydrodynamics, 29 (2017) 1–12.

[16] J. Murillo, A. Navas-Montilla, A comprehensive explanation and exercise of the source terms in hyperbolic systems using Roe type solutions, Application to the 1D-2D shallow water equations, Advances in Water Resources 98 (2016) 70–96.

[17] V. Caleffi, A. Valiani, A 2D local discontinuous Galerkin method for contaminant transport in channel bends, Computers & Fluids, 88 (2013) 629-642.

[18] W. Rodi, Turbulence models and their application in hydraulics: A state-of-the-art review. Rotterdam, Balkema - IAHR AIRH monograph series (1993).

[19] L. Cea, J. Puertas, M. E. Vázquez-Cendón, Depth averaged modelling of turbulent shallow water flow with wet-dry fronts, Archives of Computational Methods in Engineering, 14 (2007) 303–341.

[20] B. Yulistiyanto, Y. Zech, W. H. Graf, Flow around a cylinder: Shallow-water modeling with diffusion-dispersion, Journal of Hydraulic Engineering, 124 (1998) 419-429.

[21] W. Wu, P. Wang, N. Chiba, Comparison of five depth-averaged 2-D turbulence models for river flows, Archives of Hydro-Engineering and Environmental Mechanics, 51 (2004) 183-200.

[22] C. Hinterberger, J. Fröhlich, W. Rodi, Three-dimensional and depth-averaged large-eddy simulations of some shallow water flows, Journal of Hydraulic Engineering, 133 (2007) 857-872.

[23] R. C. Moura, S. J. Sherwin, J. Peiró, Linear dispersion–diffusion analysis and its application to under-resolved turbulence simulations using discontinuous Galerkin spectral/hp methods, Journal of Computational Physics, 298 (2015), 695-710.

[24] J. Macías, M. J. Castro, S. Ortega, C. Escalante, J. M. González-Vida, Performance benchmarking of tsunami-HySEA model for NTHMP's inundation mapping activities. Pure and Applied Geophysics, 174 (2017) 3147–3183.

[25] C.E. Castro, E.F. Toro and M. Käser, ADER scheme on unstructured meshes for shallow water: simulation of tsunami waves, Geophysical Journal International 189 (2021) 1505–1520.

[26] A. Navas-Montilla, J. Murillo, Asymptotically and exactly energy balanced augmented flux-ADER schemes with application to hyperbolic conservation laws with geometric source terms, Journal of Computational Physics 317 (2016) 108–147.

[27] E.F. Toro, V.A. Titarev, Solution of the generalised Riemann problem for advection-reaction equations, Proc. Roy. Soc. London A 458 (2002) 271–281.

[28] E.F. Toro, V.A. Titarev, ADER schemes for scalar hyperbolic conservation laws with source terms in three space dimensions, Journal of Computational Physics 202 (1) (2005) 196–215.

[29] E.F. Toro, V.A. Titarev, Derivative Riemann solvers for systems of conservation laws and ADER methods, Journal of Computational Physics 212 (1) (2006) 150–165.

[30] M. Dumbser, M. Käser and E.F. Toro, An arbitrary high-order Discontinuous Galerkin method for elastic waves on unstructured meshes-V. Local time stepping and p-adaptivity, Geophysical Journal International 171 (2007) 695–717.

[31] M. Dumbser, M. Castro, C. Parés, E. F. Toro, ADER schemes on unstructured meshes for non-conservative hyperbolic systems: Applications to geophysical flows, Computers & Fluids 38 (2009) 1731–1748.

[32] C.E. Castro, E.F. Toro, Solvers for the high-order Riemann problem for hyperbolic balance laws, Journal of Computational Physics 227 (2008) 2481–2513.

[33] G. Vignoli, V.A. Titarev, E.F. Toro, ADER schemes for the shallow water equations in channel with irregular bottom elevation, Journal of Computational Physics 227 (2008) 2463–2480.

[34] G. Montecinos, C.E. Castro, M. Dumbser and E.F. Toro, Comparison of solvers for the generalized Riemann problem for hyperbolic systems with source terms, Journal of Computational Physics 231 (2012) 6472 – 6494.

[35] A. Canestrelli, A. Siviglia, M. Dumbser, E. F. Toro, Well-balanced high-order centred schemes for non-conservative hyperbolic systems. Applications to shallow water equations with fixed and mobile bed, Advances in Water Resources 32 (2009) 834–844.

[36] V. Caleffi, A. Valiani and A. Bernini, Fourth-order balanced source term treatment in central WENO schemes for shallow water equations. Journal of Computational Physics, 218 (2006) 228-245.

[37] T. Schwartzkopff, M. Dumbser, C.-D. Munz, Fast high order ADER schemes for linear hyperbolic equations, Journal of Computational Physics 197 (2004) 532–539.

[38] A. Navas-Montilla, J. Murillo, 2D Well-balanced Augmented ADER schemes for the Shallow Water Equations with bed elevation and extension to the rotating frame, Journal of Computational Physics 372 (2018) 316–348.

[39] F. Jia, Z. Gao, W. S. Don, A spectral study on the dissipation and dispersion of the WENO schemes. Journal of Scientific Computing, 63 (2015) 49–77.

[40] D. S. Balsara, Efficient implementation of ADER schemes for Euler and magnetohydrodynamical flows on structured meshes–Speed comparisons with Runge–Kutta methods, Journal of Computational Physics 235 (2013) 934-969.

[41] C. Juez, I. Buhlmann, G. Maechler, A.J. Schleiss, M. J. Franca, Transport of suspended sediments under the influence of bank macro-roughness, Earth Surface Processes and Landforms, 43 (2018) 271-284.

[42] E. Godlewski, P.-A. Raviart Numerical Approximation of Hyperbolic Systems of Conservation Laws. Springer Science and Business Media, Berlin, 2013.

[43] M. J. Franca, M. Brocchini, Turbulence in rivers. In Rivers – Physical, Fluvial and Environmental Processes, Springer (2015) 51–78.

[44] E. Awad, E. Toorman, C. Lacor, Large eddy simulations for quasi-2D turbulence in shallow flows: A comparison between different subgrid scale models. Journal of Marine Systems, 77 (2009) 511–528.

[45] P. A. Madsen, M. Rugbjerg, I. R. Warren, Subgrid modelling in depth integrated flows, Coastal Engineering (1989) 505–511.

[46] J. Murillo, J. Burguete, P. Brufau, P. García-Navarro, Coupling between shallow water and solute flow equations: analysis and management of source terms in 2D. International Journal for Numerical Methods in Fluids, 49 (2005) 267–299.

[47] P.L. Roe, Approximate Riemann solvers, parameter vectors, and difference schemes, Journal of Computational Physics 43 (1981) 357–372.

[48] J.B. Cheng, E. F. Toro, S. Jiang, W. Tang, A sub-cell WENO reconstruction method for spatial derivatives in the ADER scheme , Journal of Computational Physics, 251 (2013) 53–80.

[49] C.W. Shu, S. Osher, Efficient implementation of essentially non-oscillatory shock-capturing schemes, Journal of Computational Physics 77 (1988) 439–471.

[50] S. Lardeau, M. A. Leschziner, Unsteady RANS modelling of wake–blade interaction: computational requirements and limitations. Computers & fluids, 34 (2005) 3–21.

[51] M. Thorel, H. Piégay, C. Barthelemy, B. Räpple, C. Gruel, P. Marmonier, T. Winiarski, J.-P. Bedell, F. Arnaud, G. Roux, J. C. Stella, G. Seignemartin, A. Tena-Pagan, V. Wawrzyniak, D. Roux-Michollet, B. Oursel, S. Fayolle, C. Bertrand, Socio-environmental implications of process-based restoration strategies in large rivers: should we remove novel ecosystems along the Rhône (France), Regional Environmental Change, 18 (2018) 2019–2031.

[52] Y. Akutina, Experimental investigation of flow structures in a shallow embayment using 3D-PTV, PhD thesis, McGill University, Montreal, (2015).